

**“Probing Viscoelastic Properties
of Complex Fluids by Piezo-Rheometry
in the Intermediate Frequency Range”**

Thanasis Athanasiou

Supervisors: G. Petekidis and D. Vlassopoulos

University of Crete, November 2017

Department of Materials Science and Technology

and

Foundation of Research and Technology Hellas (FORTH)

Acknowledgments

An engineer will encounter soft matter via an application. A scientist on the contrary, will study material behavior either directly (macroscopically) or (and) indirectly (mesoscopically). As an engineer I have started from applications and had the opportunity to make a fantastic “scientific” journey to the mesoscopic world of colloids and polymers, receiving answers to myriads of questions. I am really grateful to all those that made this journey feasible and contributed to its completion.

First of all would like to thank my lab mates for being always available, despite their busy schedule. I am indebted to Daniele Parisi for helping me at my first steps in TTS and providing the script to calculate the dynamic moduli from creep data. Many thanks to our intuitive technician Antonis and helpful Antje for their support.

Allan and Salvatore thank you for setting the foundations of this work. Allan also thanks for the detailed and strict guidelines on solvent washing, my first practical lesson in the lab.

I also thank Prof B. Loppinet , D. Papazoglou and G Aurenhamer for useful discussions and ideas. I could not forget to thank all material science department professors and especially Giannis Remediakis, Kelly Velonia, George Kioseoglou, George Kopidakis and Gerasimos Armatas for their “positive aurora” that contributed to my adhesion in materials science.

Finally I really appreciate all the efforts and precious time spend by my supervisors George Petekidis and Dimitris Vlassopoulos that materialized this journey and guided me towards “ergodicity”.

Table of Contents

Chapter 1: Introduction.....	1
1.1 <i>Basic Concepts and Motivation.....</i>	1
1.2 <i>Thesis Scope and Outline.....</i>	3
Chapter 2: Piezo Rheometry	5
2.1 <i>Rheometry: An overview</i>	5
2.1.1 Shear Geometry	5
2.1.2 From fluid to solid	6
2.1.3 Time Domain Characterization.....	7
2.1.4 Frequency Domain Characterization	8
2.1.5 Kramers-Kronig relations	9
2.2 <i>Inertia and Sliding Plate Geometry Physics</i>	9
2.3 <i>Piezoelectric Sensors and Actuators: an Introduction</i>	12
2.3.1 Piezo Ceramic Elements	12
2.3.2 Charge Sensing	13
2.4 <i>Piezo Rheometer Description.....</i>	18
2.4.1 Setup Overview	18
2.4.2 Technical details	19
2.4.3 Error analysis	20
Chapter 3: Materials and Rheology.....	23
3.1 <i>Brief Introduction to Polymers and Colloids.....</i>	23
3.1.1 Diffusion in the Dilute Limit	24
3.1.2 Colloidal Micromechanics and Softness of Hard Spheres	24
3.1.3 Crystallization of Hard Spheres	26
3.1.4 Colloidal Repulsive Glass.....	26
3.1.5 Colloidal Attractive Glass and Other Colloidal Glass Formers	26
3.1.6 Self Diffusion and Time scales in the Glassy State	27
3.2 <i>Linear Viscoelasticity of Linear Polymer Chains.....</i>	29
3.3 <i>Linear Viscoelasticity of Colloidal HS Glasses.....</i>	31
3.3.1 Scaling Laws at Short Times and High Volume Fractions	32
3.3.2 Criteria for onset of Non Linearity	34
3.3.3 Impact of Wall Slip on Colloidal Glass in Oscillatory Tests	34
3.3.4 Dimensionless Quantities for Oscillatory Shear	35

Chapter 4: Calibration and Validation.....	36
4.1 Calibration I : Electronic Error Compensation.....	36
4.2 Calibration II: PDMS	39
4.3 Calibration III and Validation: Linear Poly Butadiene (PBd).....	43
Chapter 5 Colloidal HS Glasses: Results and Discussion.....	48
5.1 Linear Rheology of Hard Sphere Glasses and Aging.....	49
5.2 Scaling laws above high-frequency crossover	52
5.2.1 Elastic Modulus	53
5.2.2 Viscous modulus and Dynamic viscosity.	55
5.2.3 Time scaling derived from “Trap” model	56
5.3 Extending the Low frequency end of the spectrum.....	59
Chapter 6: Conclusions and Recommendations for Future work.....	60
6.1 Conclusions from the Piezo-Rheometry study.....	60
6.2 Conclusions from the concentrated Hard Spheres study.....	60
6.3 Future Work	61
Appendix A: Photographs and Plans	62
Appendix B: Transient Tests	63
References	64

Chapter 1: Introduction

1.1 Basic Concepts and Motivation

The study and development of new materials has always been challenging and fascinating. It becomes more interesting when one departs from the bulk domain and starts penetrating into the underlying microstructure, the mesoscopic kingdom of matter. The bar is further raised when one attempts to directly relate bulk behavior with the equilibrium microstructure and single particle dynamics, an indirect albeit fundamental approach. All this scientific effort converges to the requirement for enhance predictive power and experimental verification of material behavior. Durability, toughness, high melting point, processability are some examples of desired qualities and in general the most important goal, is to develop an ability to tune the mechanical properties of matter, in order to optimize processing and enhance the range of applications.

Today metal alloys and polymers represent the work horses of applied engineering. Both classes of materials exhibit a common feature when exposed to a sequence of mechanical strains, memory. However this memory of strain history is “expressed” in a very different way and we believe sets the barrier between metal alloys and polymers, or better hard and soft matter, respectively. A metal, in its solid form, will give an instant stress response to strain, with a constant magnitude as long as the perturbation is unchanged, thus retaining a long-term strain memory. If small enough, deformation will be recoverable, hence will store all energy. The strain history footprint will be reflected as fatigue after a number of strain cycles that eventually will alter its crystal structure and mechanical properties and may lead to failure. On the other hand polymers are different. Their response to strain reflects a **fading memory** of all past applied strains. Physically, this indicates a relaxation mechanism, a time-dependent change towards a new equilibrium, involving energy dissipation. Relaxation gradually restores internal stresses (up to a limit) by local rearrangements of macromolecules or particles and is the basis of the viscoelasticity concept, that will be analyzed in chapter 2.

The fundamental process of self diffusion, due to thermal fluctuations, enhances relaxation mechanisms in both particulate and macromolecular fluids. Long-time dynamics of long (entangled) linear polymeric melts or solutions are dominated by the diffusion of the chains along their contour length, constrained by a virtual tube-shaped confinement. Similarly colloidal particles smoothen concentration and residual stress heterogeneities by self diffusion. Modeling diffusion of many-body interacting systems is still a challenge, even without considering the peculiarities of complex fluids such as stochastic motion, structural disorder, multiple relaxation processes and heterogeneities. This renders experimental characterization of soft matter viscoelasticity necessary, with material properties

that are essentially time-averaged, as measurement time scale is much longer than the microscopic dynamical one.

As mentioned complex fluids possess dynamics characterized by a distribution of relaxation times of different nature. Consequently, only broad frequency mechanical spectroscopy would directly and fully characterize this viscoelastic response, providing insight into the roles of molecular architecture and particle interactions. Many techniques are used to complement the spectrum in the intermediate and high frequencies in molecular fluids (Hecksher, Torchinsky et al. 2017) (Szántó, Vogt et al. 2017) and in colloids (Willenbacher and Oelschlaeger 2007, Mattarelli, Montagna et al. 2012). Commercial Rotational Rheometers (CRR) are very versatile, however with a limited frequency range up to 150 rad/s. The classic approach to extend this range by Time-Temperature Superposition (TTS) has its own limitations (Plazek 1996) and cannot be applied in many solutions, colloidal suspensions and semi-crystalline polymers, as temperature alters their thermodynamic state and in many cases multiple relaxation mechanism of different nature demonstrate different temperature dependence. Dielectric spectroscopy (for certain materials) and many indirect micro-rheological techniques can also access a broad spectrum. The latter provide the values of dynamic moduli indirectly from micromechanical observables demonstrating merits and weaknesses as well (Vleminckx and Clasen 2014). Time-Concentration Superposition (TCS) could also be applicable to colloids in conjunction with CRR data by overlying dynamic moduli data measured at multiple concentrations, with respect to a reference fluid concentration (Wen, Schaefer et al. 2015) but this is not always possible with particles or self-assembled microstructures that are sensitive to concentration. Last, we mention the torsional resonators which also cover a broad spectrum but require large volumes of sample and measure at discrete values for each setup although the latter restriction could be eliminated (Wang, Wang et al. 2010). Piezo-driven rheometers can complement the spectrum of CRR's. Considering that torsional resonators, diffusive Wave Spectroscopy (DWS) and Brillouin Light Scattering extend the range to higher frequencies further deep into the Giga Hertz range, we define piezo-technique as one occupying the “intermediate” frequency regime, as shown in fig 1.1 below.

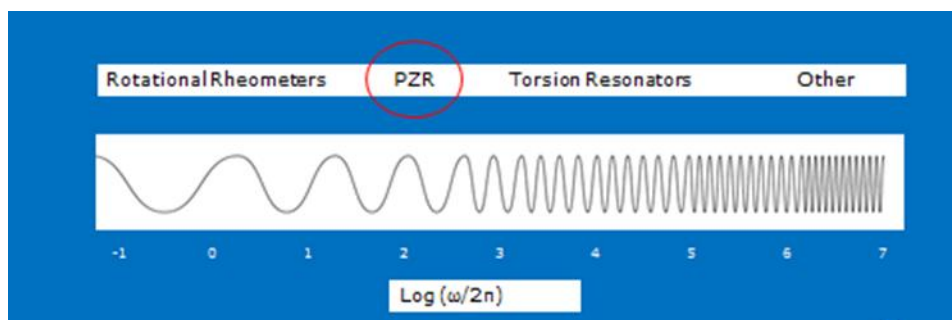


Figure 1.1: Frequency spectrum accessed by different techniques

Piezo-driven rheological measurements have been discussed in the literature dating back in the *seventies* where many innovative devices were developed, (Ferry 1980) well before the massive

production of rotational rheometers (CRR) prevail. To the best of our knowledge, the first description and use of such a device was in 1977 (Bartolino and Durand 1977) for the study of liquid crystal mesophases such as smectic A and smectic C. It was used by the Yamamoto group with similar systems in order to study the “low-frequency range of 10 Hz to 1 kHz” (Yamamoto, Nakamura et al. 1987, Yamamoto and Okano 1991). The group innovatively used pseudo-random noise to simultaneously obtain the entire frequency spectrum. In very narrow gaps ordered particles were confined to within 50 microns. Displacement was also claimed to be of the order of few tens of nm, making the setup suitable for fragile systems. Both groups used the device in dilatation mode, as it was originally designed, whereas it suffered from issues with cleronomics, (e.g. **cell rigidity**) when used in shear mode. Other groups (Martinoty, Gallani et al. 1998) contributed further to the development of the device using it in shear mode and very small gaps for linear polymers, raising concerns about confinement effects (McKenna 2006). The sliding plate cell was also modeled by a group of engineers (Sánchez, Prieto et al. 2008) validating the method in compression mode. In 2010 Martinoti was granted a US patent for his design. The same year the setup was used in shear mode in order to study the mechanical solidification of liquid crystal-colloid composites (Roth, D’Acunzi et al. 2010). Finally, it should be stressed out that many groups have developed similar devices for high frequencies such as mechanically oscillating parallel plates (Eggers and Richmann 1995) or piezo-rotating parallel disks (Kirschenmann and Pechhold 2002).

1.2 Thesis Scope and Outline

In this study we revisit and improve the technique and its implementation, discuss the various problems and remedies and apply to glassy hard sphere colloids and entangled linear polymers melts and solutions. Both systems exhibit rich dynamics, in the probing range of 20-1000 Hz due to beta relaxation (in-cage rattling) and fluctuations of strands between entanglements, respectively. Comparison against data obtained with conventional rotational rheometers at overlapping frequencies is very satisfactory, validating the technique. Further validation is accomplished by comparison against TTS data for the linear polymer samples. Features like the low sample volume required, the extensive frequency range, the imposed rectilinear flow and the small applied deformation - critical for potentially fragile systems - are among some of the vital characteristics that prove this technique a valuable tool, in probing the linear mechanical response of soft matter systems.

This thesis is twofold reflecting the study of the technique and the system. Engineering terminology is kept as simple as possible, stripped from unnecessary details that can be found in References. The outline is as follows:

Chapter 2 is devoted to the instrument and the technique. Section 2.1 provides background on oscillatory rheometry, starting from basic principles and fundamental material properties, which are needed in order to characterize complex fluids. Section 2.2 enlightens the physical principles of

sliding plate geometry in the high-frequency region. Section 2.3 provides background on piezoelectric principles (technical) while the setup and its limitations are presented in the next two sections 2.4 and 2.5.

Chapter 3 is system-oriented. Section 3.1 is an introduction to linear polymeric melts and near-hard sphere colloidal glasses. It focuses on the microstructure and micromechanics, an important concept for the analysis of rheological data although the resulting signature cannot always be detected in bulk rheology. In 3.2 discussion of polymer rheology is limited to entangled melts and solutions, tunable by observation time, temperature and number of entanglements per chain. Colloidal glass rheology in 3.3 is more extensive focusing on the expected behavior around the high frequency or cage crossover.

Chapter 4 reports and discusses calibration methods. During the analysis we study primary magnitude and phase angle of the sinusoidal stress response as functions of frequency. For a rheologist it might seem counterintuitive, however these are the parameters that the instrument “feels” thus their divergence from the expected value reflects directly the underlying cause.

Chapter 5 is the distillate of this work, presenting measurements with colloidal glasses and comparison with theoretical or empirical scaling laws. Here, time dependence and viscous and elastic component limiting behavior as functions of volume fraction are studied.

Finally, **Chapter 6** concludes and gives an insight into future work.

Chapter 2: Piezo Rheometry

2.1 Rheometry: An overview

Rheometry is a measuring technique for determining the rheological properties of a material. By definition, rheology is “the study of flow and deformation of materials”. One could add “...at different time scales” to emphasize the concept of time in rheological observations. Given considerable enough time almost everything will eventually flow and here comes the pitch drop experiment to demonstrate it (Edgeworth, Dalton et al. 1984).

Rheology correlates the history of deformation and its time derivative to stress response, which in turn is related to the underlying microstructure i.e. the spatial distribution of particles. Polymers and colloids, when stressed or deformed, exhibit a unique behavior compared to metals, defined as viscoelasticity. This behavior can be viewed as a memory over the past imposed perturbations that decay over time, as will be discussed below. A solid metal alloy or water, would theoretically exhibit an eternal and instant relaxation, respectively. Understanding relaxation is essential in our study.

Shear is the most widely used perturbation (flow) to probe the rheological behavior and (indirectly) structure of complex fluids and thus discussion will be limited to uniaxial shear stress referred as *stress*. Stress drives deformation. Alternatively if deformation is applied the material will respond with stress. In Rheo-metry we define stress-control and strain-control deformations. In this study we will focus on *strain control* unidirectional isochoric shear flow. The 2D governing equations are relatively simple. Stresses for all planes and axes can be condensed within the second order stress tensor ($\underline{\underline{\sigma}}$). Rheological symbols used below comply with the official symbols and nomenclature of The Society of Rheology (2013). More on definitions, principles and tensorial notation can be found in many textbooks (Morrison 2001) (Macosko 1994).

2.1.1 Shear Geometry

Fig 2.1.1 illustrates the basic planar Couette flow geometry, the sliding plates. Being so elementary is an ideal case study for rectilinear shear flow. The sample is confined between two surfaces defined as the moving and the standing or, better, reflecting surface. Assuming the top plate is moving with constant velocity V_0 , a planar shear velocity gradient is set in the gap d between the two surfaces. Quantitatively the perturbation is described by strain (γ), the ratio of the shear amplitude (at time t) to the gap d and the shear rate, its first derivative in respect to time ($\dot{\gamma}$). Material response $\sigma(t)$ is picked up on the standing plate by a stress sensor. In practice, the sensor measures the force (F) magnitude that is then divided by the sample cross section (plate area). Proper notation requires “21” as subscripts in stress and strain to indicate shear plane and its axis thus we write σ_{21} and γ_{21} .

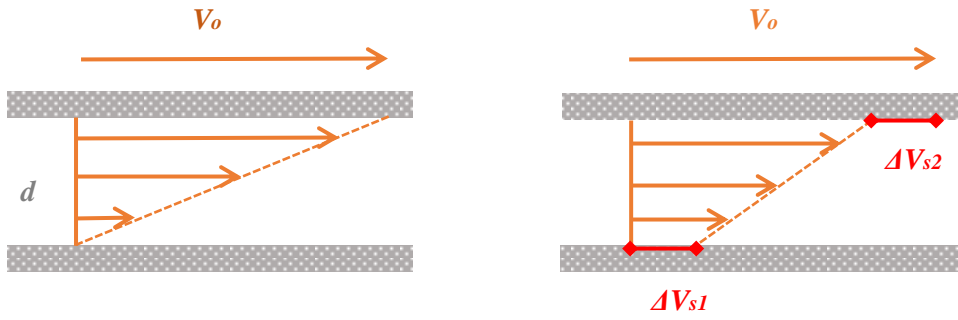


Figure 2.1.1 Sliding plate geometry with the upper plate moving and the lower stationary. Left: Ideal planar Couette flow. Right: Same with wall slip

Ideally we assume no-slip boundary conditions while in practice wall slip can occur as shown in fig 2.1.1 (right) - and become important under certain conditions - where the “upper” layer of fluid is moving with velocity $V_0 - \Delta V_{s2}$ and the lower (supposed standing) with ΔV_{s1} . The mechanism of slip and the effects in rheology strongly depend on the material (molecular or particulate) and the test parameters (Hatzikiriakos 2015, Cloitre and Bonnecaze 2017). It will be further discussed in the next chapters.

2.1.2 From fluid to solid

Momentum conservation dictates that fluid flow, via a tube for instance, is governed by viscosity, whereas according to Hooke’s law deformation of a solid is governed by elasticity. A *perfect fluid* is referred as Newtonian: When mechanical stress is applied deformation rate follow Newton’s law. This purely viscous behavior dissipates energy due to the work spend to flow only partly which is converted to thermal energy (viscous heating) and cannot be recovered to its mechanical form. Density (ρ) and viscosity (η) contain **all material information necessary** to predict its flow governed by conservation of mass and momentum principles.

$$\text{Newton's law in simple form: } \sigma_{21} = \eta \cdot \dot{\gamma}_{21} \quad (2.1)$$

On the other hand a *perfect solid* has pure Hookean behavior: When mechanical stress is applied its maximum deformation follows Hooke’s law. Deformation process is purely reversible so we consider the work spent to be stored and released when returned to equilibrium. In this case mechanical response is governed by the modulus G , a constant material property when perturbation is well below yielding.

$$\text{Hooke's law: } \sigma_{21} = G \cdot \gamma_{21} \quad (2.2)$$

Ideal cases exist only in theory. Even water does not always behave like pure fluid and steel can exhibit dissipative behavior when a stress wave propagates through its lattice. This is the reason we define viscoelasticity (VE) to describe the behavior of real materials that respond partly like solids and partly like liquids in various proportions. A *viscoelastic material stores* part of the mechanical

energy elastically, and dissipates the rest simultaneously through viscous relaxation. Viscosity is a function of shear rate, calling for more parameters for complete characterization.

2.1.3 Time Domain Characterization

Relaxation reflects the feature of materials presenting partial fading memory over all strains applied and this is the essence of viscoelasticity. By extending Newton's law in tensorial form and by adding memory contribution (term in brackets), we can describe stress at time t for a fluid with fading memory (Morrison 2001)

$$\underline{\underline{\sigma}}(t) = - \int_{-\infty}^t \left[\frac{\eta_0}{t_0} e^{-\frac{(t-t')}{t_0}} \right] \underline{\underline{\dot{\gamma}}}(t') dt' \quad (2.3)$$

Theoretical studies and modeling of viscoelasticity are based on elastic (springs) and damping (dashpots) elements considered in Maxwell and Voight-Kelvin models, which were later enriched with numerous elements (Rubinstein and Colby 2003). The bracket term above derives from the Maxwell model providing a mathematical representation of relaxation time t_0 .

Following an instant (impulse) deformation, rearrangements could take place within finite relaxation time. A real material's VE relaxation function should decrease monotonically in time, as strain is being forgotten. Although true impulse functions do not exist in nature, their superposition can represent any arbitrary function and thus model the response of a causal linear system. Theoretically a linear time invariant system's response $\sigma(t)$ to an arbitrary excitation $V(t)$ can be calculated by convoluting the input to its impulse response $\Psi(t)$ which can be obtained by differentiating the step response as shown in fig 2.1.2.



Figure 2.1.2 Linear Time Invariant System response

This proves that **all information** regarding a system's linear response is contained in a step response function, say $G(t)$. Suppose a sudden (step) shear strain γ_0 is applied at time $t=0$ to a material. The time-dependent relaxation modulus, a ratio of stress response over imposed strain can be defined: $G(t) = \sigma_{21}(t, \gamma_0) / \gamma_0$. In light of the above, $G(t)$ is a fundamental material property characterizing viscoelasticity. It could be measured directly by performing a step strain experiment, where an "instant" strain is applied and the response is plotted over time. In practice, it is not possible to measure the relaxation modulus over the entire time spectrum with sufficient accuracy. The "Instant" strain is never instant and tracking the relaxation at small and long times is challenging. Ideally, with infinite measuring points one can describe the continuous time span $H(t)$, which is very often represented by a stretched exponential function containing relaxation time t_0

$$G(t) = G_{\infty} + G_0 \exp[-(\frac{t}{\tau_0})^{\beta}] \quad (2.5)$$

with G_{∞} and G_0 representing the modulus when $t \rightarrow \infty$ and $t \rightarrow 0$, respectively and β a fitting (shape) parameter. The stretched exponential function fits many relaxation processes in disordered molecular systems although it is widely believed that there is no physical microscopic basis in molecular relaxation.

2.1.4 Frequency Domain Characterization

To overcome step-strain difficulties, especially at short times, one needs to use dynamic or better sinusoidal excitation methods, thus moving from time to frequency resolved methods. Any LTI system can be characterized in the *frequency domain* by its transfer function, which is the Laplace transform of its impulse response. Mathematically, sinusoids are a sum of complex exponentials with complex-conjugate frequencies suggesting the output of the system will also be a sinusoid, with a different magnitude and phase but on the same frequency upon reaching steady-state. This is the origin of the concept that a periodic experiment at frequency ω , is qualitatively equivalent to a transient at $t=1/\omega$ where a quasi steady-state is reached within one period of oscillation (Ferry 1980). Naturally $G(t)$ can be viewed as a distribution of relaxation times as proposed by Wiechert in 1893 in his classic studies of the "elastic after-effect" (Tschoegl 2012). The basis is Boltzman superposition principle stating that the effects of mechanical history are linearly additive.

Consequently we vary the observational time (τ_{exp}) window, by sweeping the frequency range. This time scale sets the minimum **time resolution** of an experiment and observables i.e. mean squared displacement (MSD) are averaged over the time interval that sets the time scale (Dhont 1996). Dynamic oscillatory tests data are reported in terms of dynamic moduli, the elastic G' and viscous G'' , at discrete frequencies. As the excitation varies in time $\gamma(t) = \gamma_0 \sin \omega t$, the elastic part of the material responds instantly to deformation $\gamma(t) : \sigma'(t) \sim G' \gamma_0 \sin \omega t$. The viscous part will feel and respond only to its time derivative ($\dot{\gamma}$) : $\sigma''(t) \sim G'' \gamma_0 \omega \cos \omega t$. From the above we extract that the elastic response is in phase with strain and the viscous is advancing 90° . As the two strain functions are orthogonal, we can use complex notation and define the complex modulus (G^*) and complex viscosity (η^*) and their real and imaginary components G', G'' and η', η'' respectively. It can be shown that dynamic moduli can be represented by the discrete Fourier transformations of the relaxation modulus where the variable $S=t-t'$ with t' an arbitrary time.

$$G'(\omega) = \omega \int_0^{\infty} G(s) \sin(\omega s) ds \quad \text{and} \quad G''(\omega) = \omega \int_0^{\infty} G(s) \cos(\omega s) ds \quad (2.6)$$

The above equations suggest that dynamic moduli could be calculated if the full relaxation spectrum $H(t)$ is known or dense measurements of $G(t)$ are made over an extensive frequency range (Winter 1997). Consequently, the **complex modulus** $G^*(\omega)$ contains all needed information in order to characterize the linear viscoelastic properties with polar components magnitude and phase, being the

fundamental parameters that bulk rheometers measure. All other dynamic parameters can then be calculated.

2.1.5 Kramers-Kronig relations

In the next few lines of this section we will provide the background for Kramers-Kronig (KK) relations. The ubiquitous principle of causality states : The same cause or set of causes always produces the same effect or effects (other things being equal) and the cause(s) temporally precedes, or is simultaneous with, its effect(s) (Riggs 2009). Causality and linearity are prerequisites for KK relations to hold for dissipative systems. Although initially developed for causal optical systems, the theory leads to the interrelation of G' and G'' , conveying the causality condition:

$$\frac{G'(\omega)}{\omega^2} = \frac{2}{\pi} \int_0^{\infty} \frac{G''(\chi)}{\omega^2 - \chi^2} dx \quad (2.7)$$

The implementation of the above equation 2.7 is not feasible as it requires almost infinite data spectrum. However, it has been theoretically shown that the discrete relaxation modulus expressed as a sum of exponential decays (Maxwell modes) will always satisfy KK relation (Winter 1997). Since this interconnection exists, magnitude and phase could also be interrelated:

$$\delta(\omega) \cong \frac{\pi}{2} \frac{d \ln(|G(\omega)^*|)}{d \ln(\omega)} \quad (2.8)$$

The above approximation (Booij and Thoone 1982) will be tested and used to improve accuracy as will be discussed in section 4.4. We need to mention that there are arguments why this approximation introduces noise. Another group (Parot and Duperray 2007) developed a more complicated algorithm and showed that it eliminates noise from calculated δ values. It was later used to enhance accuracy in TTS data for amorphous polymer (Rouleau, Deü et al. 2013). The integral ($G''(\omega)$ over time) method, used in entangled polymeric chains to calculate the plateau modulus is another proof of the validity of KK relation in linear systems (Liu, He et al. 2006). In this work we will use the simple approach of Booij and Thoone (equation 2.8).

2.2 Inertia and Sliding Plate Geometry Physics

Any kind of periodic motion involves inertia. There is tool (plates) inertia and sample inertia. The first is of no concern for CRR users as the instrument auto compensates up to a point. Even resonances are compensated in modern instruments by the induction of an active counter signal. Sample inertia also rarely dominates up to 150 rad/s, the usual upper limit for a Rheometric CRR. In any geometry, rotational or sliding, we can measure the response at the standing or moving surface a configuration called separated motor transducer (SMT) or combined motor transducer (CMT) respectively. Our sliding plate geometry resembles a SMT configuration where tool inertia is less important (Läuger and Stettin 2016). SMT is suited for true strain-controlled tests and performs better

than CMT at short times, suffering less from inertia (Macosko 1994) therefore we will use for data comparison, TA Instrument's ARES rheometer series and Anton's Paar MCR 702 (twin motor configuration) in SMT mode. Considering sample inertia we shall provide background on the governing physical principles in the gap looked at earlier publication.

All real materials are deformable and possess mass hence they transmit mechanical waves. During the oscillatory excitation a propagating transverse wave is created. It is also referred in seismology as an S wave, S standing for secondary as it propagates slower than the longitudinal primary (P) one (Müller, Weber et al. 2007). For rheology, we can consider it as a shear wave.

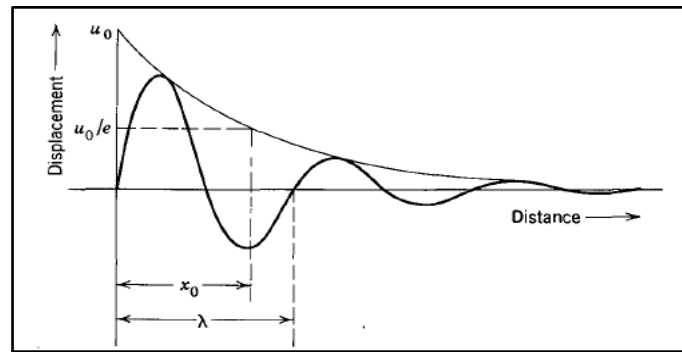


Figure 2.2.1 An attenuating and propagating transverse wave traveling through the gap with wavelength λ (Ferry, 1980)

It can be shown that the velocity of propagation of the mechanical disturbance always assumes the form of the square root of the ratio of a parameter corresponding the resistance to deformation and a parameter proportional to the inertia of the medium thus inertia is somehow related to the wavelength (λ). Figure 2.2.1 shows a transverse wave with wavelength λ , damped by the viscous element of the propagating medium in our case the sample. When the gap d is considerably larger than the wavelength, the perturbation is attenuated before reaching the measuring surface. In this case measurement is feasible only at the moving surface, the working principle of torsion resonators operating in discrete frequencies. By decreasing d around λ a standing wave is formed, from the multiple reflections in the gap, setting a complex shear velocity field. Inertia dominates and the shear history of the sample is uncontrollable. It is only when the gap is set well below the wavelength λ , referred as the Gap Loading Limit, that measurements in the standing plate are reliable (Schrag 1977). By calculating the wavelength one can define the maximum gap, which must be well below $\lambda/10$. Schrag calculated the propagating wavelength as a function of angular frequency (ω) and loss angle (δ):

$$\lambda = \frac{1}{\cos \frac{\delta}{2}} \left(\frac{|G^*|}{\rho} \right)^{\frac{1}{2}} \frac{2\pi}{\omega} \quad (2.9)$$

Based on Schrag's calculation and requiring gaps $d < \lambda/10$ the above equation can be simplified (Bharadwaj and Ewoldt 2015) setting approximate criteria for the maximum usable frequency, related to certain gap and sample density (ρ):

$$|G^*| > \frac{100}{(2\pi)^2} \omega^2 \rho d^2 \quad (2.10)$$

Shear wave is a needed concept to model sample inertia. Equation (2.10) is based on this model and defines the inertia high frequency limit and as such we expect inertia effect to be related to specific weight which is contained in the equation by sample density (ρ). Strangely, the deformation amplitude is not in the formulae, at a first glance however it is hidden behind the requirement for equation (2.11) to hold reflecting linear response (regime).

$$\eta^* = \frac{G^*}{\omega} \quad (2.11)$$

By plotting the modulus G^* versus ω in the double logarithmic plot (figure 2.2.2) one can graphically represent the HF limit. For every ω_{\max} there is a d_{\max} that can be used for a given sample. It is worth stressing that even for gaps equal to $\lambda/10$ the δ deviation could be 7.6° and 0.8° for liquid and solid samples, respectively (Schrag 1977), a considerable error taken into consideration the $\tan(\delta)$ sensitivity close to 0° and 90° deg. (Velankar and Giles 2007).

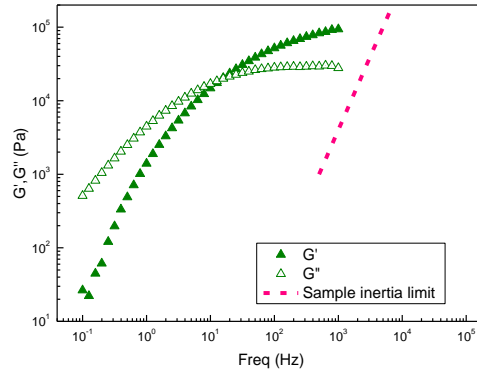


Figure 2.2.2 Inertia limit (dashed line) calculated from equation (2.10) for samples with density $\sim 1\text{g/cm}^3$ and a gap of $200\mu\text{m}$. Green symbols show a typical DFS plot of PDMS sample AK1000000.

Interestingly, the shear wave approach describes also the requirement for plates to be parallel. Mode conversion occurs when a wave encounters an interface between materials of different acoustic impedances and the incident angle is not normal to the interface (Dieulesaint and Royer 1980). Fig 2.2.3 shows an example of a longitudinal wave been reflected at a liquid-solid interface. Part of it continues its propagation in the solid (measuring plate) with a transverse component related to the angle of incidence (left). All components vanish at 90° (right). Further analysis is beyond the scope of this work, however it would be interesting one to study the wave patterns set in oscillating cone-plate geometries based on the above concept. This could determine the dependence of δ error on cone angle when cone-plate geometries are used in elevated frequency oscillatory tests (Lauser and Stettin 2016).

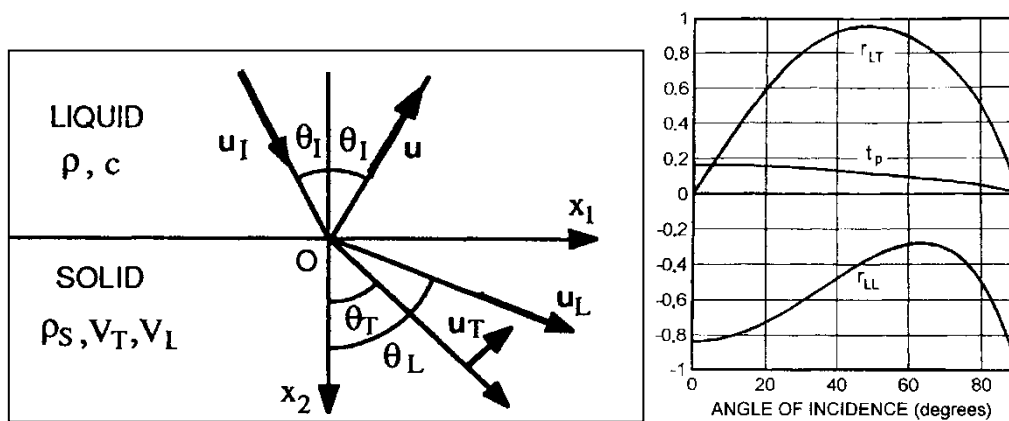


Figure 2.2.3 Left: Interface between an isotropic solid and liquid, with longitudinal wave incident in the solid. Right: The coefficients for reflection (r_{LL}), conversion into transverse (r_{LT}), and for transmission into the liquid, (t_p) (Elastic waves in solids, Royer-Dieulesaint, Springer (1996.).

2.3 Piezoelectric Sensors and Actuators: an Introduction

By applying strain to a piezo ceramic element, electric dipoles are deformed generating electric charge q . This can be measured at the electrodes by voltage sensing devices as seen in fig 2.3.1. By utilizing this principle we can use piezo ceramics as strain / stress sensors, the equivalent of a transducer in conventional rotational rheometers.

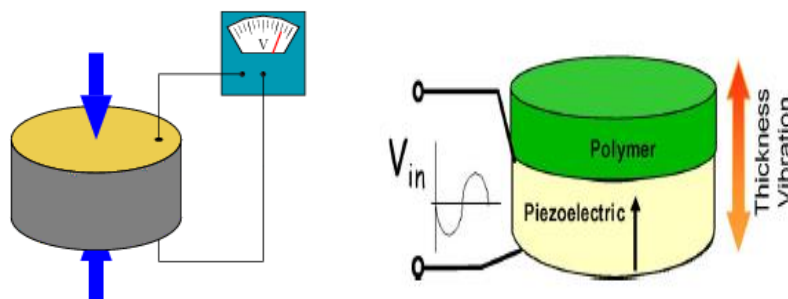


Figure 1.3.1 The direct (left) and inverse (right) piezoelectric effect (Sánchez et al 2008)

The inverse effect allows us to use the piezo ceramics as actuators (motor equivalent) that will impose the commanded displacement to the sample responding to the applied time-varying voltage. By confining the sample between the two ceramics, the actuator and the transducer, one can apply strain and sense material's response constituting a fundamental sliding plate Piezo Rheometer (PZR).

2.3.1 Piezo Ceramic Elements

Piezo ceramics are the heart of our shear cell, so their working principles and characteristics should be discussed. We use lead zirconate titanate polycrystalline ceramics in stack arrangements (referred to as PZT). In an arrangement, multiple layers are placed mechanically in series and wired in parallel achieving larger displacement. We chose this type (PZT) because of its performance in

submicron resolution actuation, fast response times and high sensitivity. The most important characteristics can be seen in the table 2.3.1 below for three types of elements manufactured by PI Ceramic GmbH, Germany. Our two Piezo-Rheometers PZR1 and PZR2 use P-141.05 and P-141.10 respectively, all being active only in X axis (shear mode). Type P-141.03 was used by Roth et al (2010) and is listed for comparison.

Type	Disp. ΔL at 250V (μm)	Dimensions (mm)	Stiffness (N/μm)	Capacitance (nF)	Resonance frequency (kHz)	Used
P-141.03	3	10X10X5.5	490	17	210	Roth et al, (2010)
P-141.05	5	10x10x7.5	360	28	155	Our PZR1
P-141.10	10	10X10X12	230	50	100	Our PZR2

Table 2.3.1 Basic characteristics of the used piezo ceramic stacks

Important characteristics are the following: a) Displacement which is of the order of a few micrometers, yielding strains ($\Delta L/d$) in the order of 0.001% for a typical gap of 200 microns and 20V (peak to peak) excitation. Large displacement is desirable for actuators with a reduced stiffness and resonance frequency as a tradeoff. In sensors displacement is reflected in sensitivity. b) Stiffness of the sensor (transducer) that limits its movement during measurement. “Standing” plate should be still but in practice this is not absolutely true introducing errors. In literature the transducer stiffness is described with its reciprocal quantity, compliance. It is compensated in commercial rheometers by means of force rebalance that could be applicable also to piezo transducers with proper electronics and optical displacement sensors via a feedback loop. c) Resonance frequency which governs the high-frequency limit and the time response of the piezo. When approaching resonance frequency the piezo element exhibits large resonating strain a phenomenon that can be understood as strain magnification due to the accumulation of input energy. Even in the worst case of P-141-10, the 100 kHz resonant frequency, is way above our working spectrum and seems not to interfere with our measurements.

2.3.2 Charge Sensing

The use of any instrument to sense the output of a transducer, would add a voltage drop as the instrument load impedance will be connected in parallel with the piezo, spoiling the measurement. Thus, a voltage to charge converter-amplifier is placed before the detecting device (oscilloscope) in order to achieve “better” linearity.

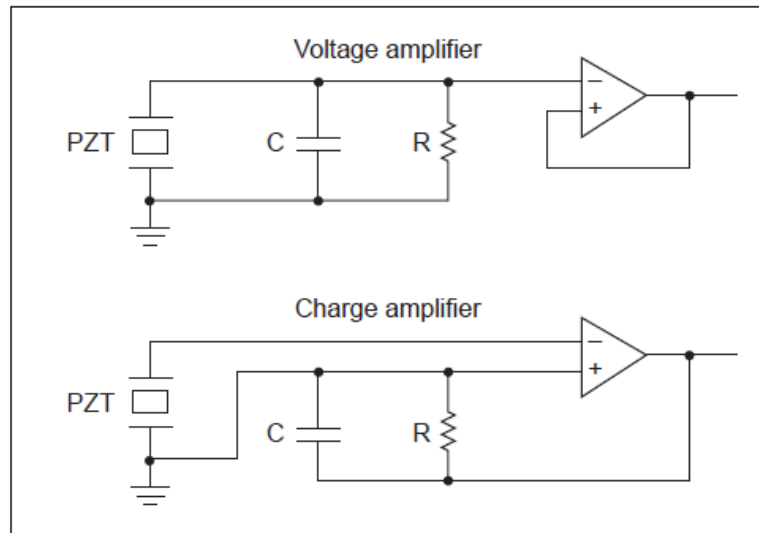


Figure 2.3.2 Charge versus voltage amplifier from *Signal Conditioning & PC Based Data Acquisition Handbook, IOTECH, 2014.*

Figure 2.3.2 illustrates the basic difference, in principle, between charge and voltage amplification. In the former case (upper circuit) the signal has to charge the capacitor C before detection, causing significant drain via resistor R. Then the operational amplifier multiplies the signal. In the latter case the capacitor is connected to Operational Amplifier (triangular symbol) positive feedback loop minimizing drain. An output voltage is generated proportional to the integrated input current also proportional to the charge $Q(t)$ divided by the capacitance C . In our Charge Amplifier capacitor C is set by the factory and cannot be adjusted. In most setups, the capacitor is connected to the inverse (-) feedback loop to enhance stabilization and linearity sacrificing the gain, the ratio of output over input. The principles of operation can also be found elsewhere (Bard 1980) section 15.2 .

The charge amplifier has two drawbacks. First it acts like a high-pass filter with lower corner frequency $f = 1/(2\pi RC)$, creating a trade-off between sensitivity and frequency response. Reducing C increases sensitivity, but it also increases the lower corner frequency. Estimating leakage resistance of the order of $10\text{ G}\Omega$, combined with a capacitance of several hundreds pF, gives a time constant of the order of a few seconds. Now it is clear that by using charge amplifier configuration, PZT sensors can only be used for dynamic and not steady measurements. This is important as it imposes the limitation: There is a time constant of the order of a few seconds (in time domain) or a low cut-off frequency (in frequency domain) that depends on the setup characteristics. This defines the low-frequency limit set for our **purpose to 10 Hz**. Second, as any electronic circuit with passive filters induces a phase and gain error. By feeding a sinusoidal signal to the charge amplifier via a capacitance equal to the piezo element value, one can measure the phase and gain response and thus the Charge Amplifier Induced Error. We have found that the gain (corresponding to $|G^*|$) error is negligible when the phase (δ) error could reach up to 50° ! Figure 2.3.3 denotes indicative phase error versus frequency for 1 kHz High-

cut filter setting. Relevant curves are provided in the brochure by the manufacturer with a lot less resolution.

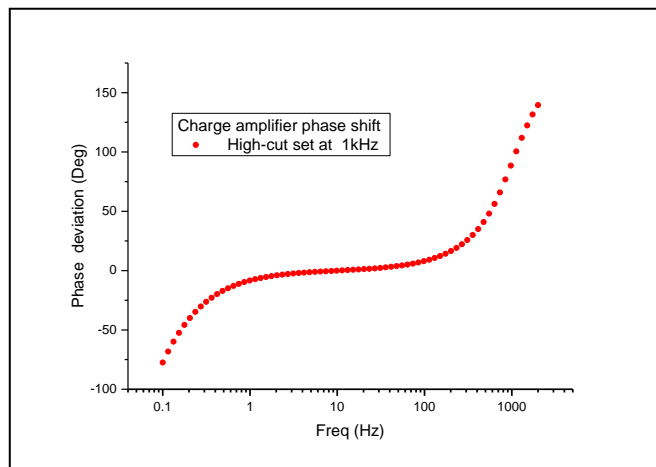


Figure 2.3.3 Data for our M-68 charge amplifier induced phase error for high-cut filter setting at 1kHz

Ferromagnetic **hysteresis and creep** affects actuator response. We will consider the actuators case although similar principles apply to sensors. When an electric voltage is applied the actuator responds with a displacement (ΔL) resulting in strain ($\Delta L/L$). The field is alternating causing proportional (to voltage) mechanical vibration. This extremely simplified concept is described by the following equation very often seen in brochures and publications.

$$\Delta L = d_{15} \cdot V \quad (2.12)$$

The subscript index 15 of the piezoelectric constant d conforms to IEEE standards and derives from the theory of piezoelectricity (Preumont 2006), (Sirohi and Chopra 2016). It indicates the axis of deformation with respect to the electric field planes. Values (15, 24) and (31, 32, 33) relate to shear and normal forces, respectively. In practice, this simple equation rarely holds due to two major weaknesses of piezo actuator hysteresis and creep introducing nonlinear response. Hysteresis means that for the same voltage excitation, the actuator may exhibit different displacement values due to different excitation history. It is generally attributed to molecular friction at regions of piezo-crystal imperfections (El Rifai and Youcef-Toumi 2004). It resembles the rate-independent memory of previous displacement history although a rate-dependent mechanism has been suggested. For operation well below the resonance frequency, the hysteresis loop is mainly affected by voltage (displacement) and load.

Fig 2.3.4 shows a typical hysteresis loop for a given actuator at small and large deformations. Hysteresis can be characterized by center point and average slope of the loop. The load can change the slope (tilt) while decreased voltage amplitude will minimize its width. Note how hysteresis is reduced for stack actuator operated at 300 Hz (sinusoidal signal) when the amplitude is decreased.

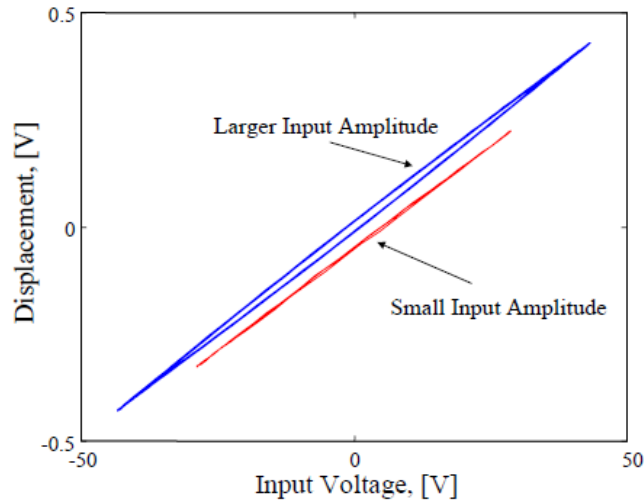


Figure 2.3.4 Hysteresis measurements at 300 Hz for piezoelectric actuator tube From Rifai et al (2004)

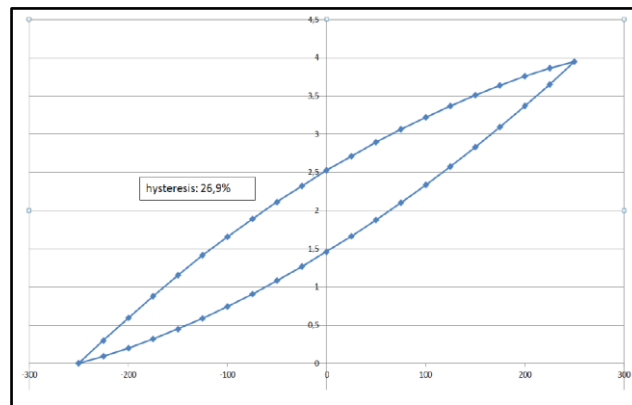


Figure 2.3.5 Hysteresis (voltage /displacement) measurements of similar to our piezo PI 153.03 capable of x,y,z axis displacements. (Measurements by PI).

Measurements made by the manufacturer (PI) with a similar to ours piezo element show that at maximum displacement range hysteresis can climb up to 26,9 % as seen in fig 2.3.5. No data for lower voltages are available. A feedback loop circuitry can also be used to tackle hysteresis however in our case it may introduce unwanted harmonics especially at high frequencies. Another method is charge control of the actuator – an analogue to charge sensing we use - as explained by (Yi and Veillette 2005) and further studied by (Bazghaleh, Grainger et al. 2014). Charge control is claimed to further improve linearity of the actuator, especially if combined by a charge feedback loop (Chen, Yen et al. 2013). Such a device is not available commercially. Simpler charge controllers are available but their specifications were not compatible with our setup (PI) while other similar devices from other companies have been discontinued. However we believe that an optical vibro-meter can verify the displacement over time of the moving plate, thus confirming the sinusoidal imposed strain. Hysteresis can limit the high-end of the usable bandwidth by inducing errors in phase and amplitude. Bode plot in fig 2.3.6 from (Wang, Chen et al. 2015) indicates the phase and gain response for a *typical* piezo actuator, from simulations and experiment. In this example errors take place at a frequency as low as 80 Hz as the first resonance frequency is extremely low. Although this is a completely different

actuator, the negative sign in phase response provides a qualitative indication of the effect of hysteresis. Again, phase is a very sensitive parameter and the above suggest a theoretical offset of our measurements towards lower δ values. Hysteresis is very well studied and modeled (Wang, Pommier-Budinger et al. 2014) meaning that with proper engineering could be eliminated. In our case an unwanted effect could be the distortion of the sine curve inducing harmonics. Our approach has been kept simple: operate at least one order of magnitude below the maximum voltage and resonance frequency.

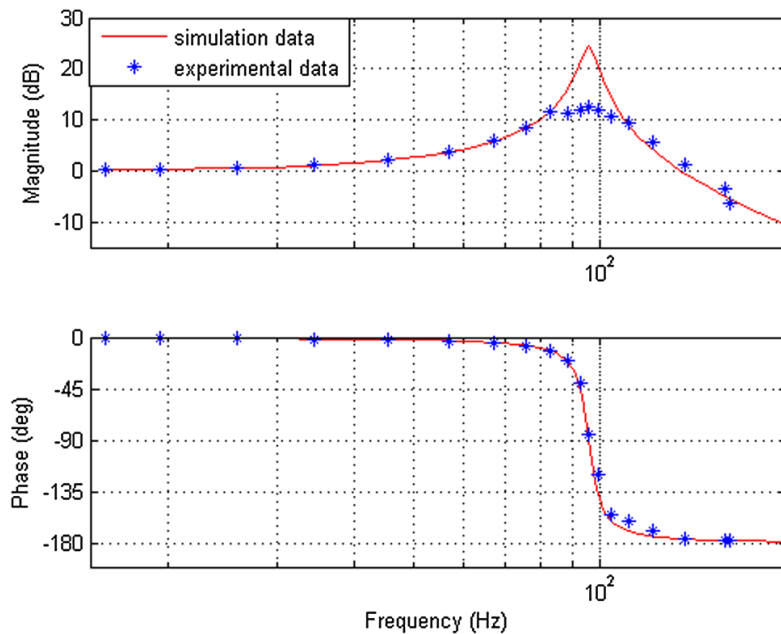


Figure 2.3.6. Typical phase and gain response (Bode) plots of piezo actuators deriving from simulations and experiments. From (Wang G. et al, 2016)

Ferroelectric creep on the other hand, can be seen as a slow drift in the PZT displacement after responding to a sudden change in the input voltage. It is the result of remnant polarization which continues to change after the applied signal reaches its maximum value. Ferroelectric creep comes into play in slow dynamics imposing a low frequency limit for PZT actuators (Nemirovsky, Nemirovsky et al. 1996) . Operating actuators fast enough we reduce the drifting caused by the creep effect. This is why we have defined 10Hz as the low-limit in our frequency range and we believe that no soft material creep test is possible with sufficient accuracy unless active control is used.

Summarizing key points

- Hysteresis may affect measurements by increasing phase angle. Using small excitation voltages we minimize the effect.
- Slow dynamics measurement is not the strong point of PZR due to creep and charge leakage in the sensor circuit.
- There is always a trade-off between sensitivity / displacement and measurement accuracy.

2.4 Piezo Rheometer Description

2.4.1 Setup Overview

A typical Rheometer setup should consist of a measuring cell, an excitation unit and a signal processing unit. A signal generator is used to excite the moving plate of the measuring cell. In our PZR case materials response (stress) will be felt on the measuring plate generating proportional electric charge. A charge amplifier will convert the charge signal to proportional time varying voltage signal, before it is fed into a measuring device (oscilloscope or lock-in amplifier) and the basic parameters, RMS voltage and phase are extracted. These correspond to G^* polar components (magnitude $|G^*(\omega)|$ and $\delta(\omega)$) hence characterizing the LVE properties of the material. By varying the measuring frequency from a min to a max value and taking measurements at certain points we can perform dynamic frequency sweep test (DFS). This is the goal of this work.

Two measuring cells (MC) were constructed. The first PZR1 was based on (Roth, D'Acunzi et al. 2010) and the second on (Yamamoto, Nakamura et al. 1987), as shown in Fig 2.3.7. The heart of the Measuring Cell consists of two piezo-elements (PICATM -Shear Piezo Actuators) the one used as an actuator thus glued to the moving plate and the other as a transducer glued to the measuring (standing) plate. The other side of each element was glued to a thick holder plate. The two holder plates are kept at certain distance and orientation (parallelism) via three bolts and tree adjusting fine threaded screws. The goal of this design is to ensure that the sample is properly placed between the moving and measuring plates while the plates are kept parallel with a fixed gap (d).

As expected the actuator element is electrically connected to a signal generator providing up to 20V peak-to-peak (PP) time-varying excitation signal $V(t)$ yielding to proportional shear displacement $\gamma(t)$. With the above proportionality assumption one can control the induced shear profile to perform **strain-controlled** oscillatory tests, step-strain and constant shear rate tests utilizing sinusoidal, pulse or ramp waveforms, respectively. We mainly used sinusoidal settings as oscillatory tests are of our main concern.

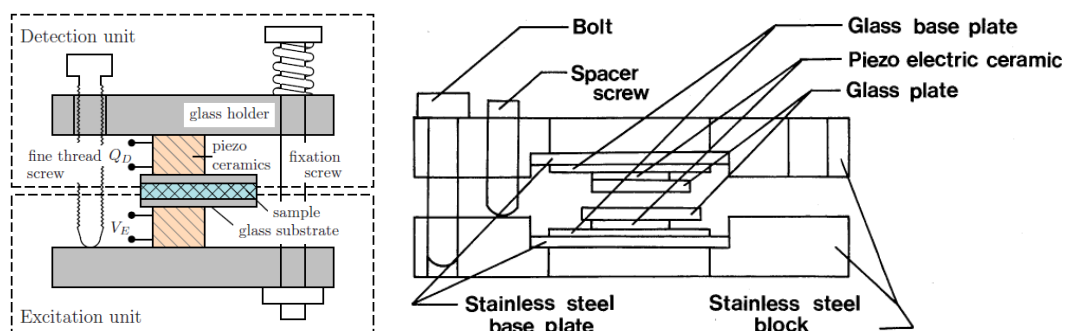


Figure 2.3.7 PZR setups in literature Left: from Roth et al,(2010) Right :from Yamamoto et al,(1987)

2.4.2 Technical details

We now discuss in more detail the setup and procedures.

2.4.2.i PZR1 and PZR2 Measuring Cell

PZR1 piezo holder plates are made of quartz glass 20mm thick. Moving and standing plates are made of the same material. Due to its superior young modulus it performs exceptionally, but machine processing is impossible without specialized equipment. Gap is set by 3 fine thread screws. PZR2 round holder plates are stainless steel and aluminum allowing the construction of a recess to house piezo ceramics and cables for better shielding. Moving and standing plates are optical grade BK7 3mm glass windows with superior flatness. One plate carries antireflection coating for 630 nm light to enhance optical alignment method. The merits of PZR2 are machinability, low cost, improved shielding, optimized optical alignment and optical grade flat sample plates. Besides, it demonstrates 10X sensitivity due to increased cross section of sample and piezo amplitude.

2.4.2.ii Excitation Unit and Signal Processing

The Excitation Unit in our case is a TG1010A frequency generator with programmable features. Although the device could be computer controlled via IEEE488 GPIB interface, we preferred the manual setting in order to have better control of the procedure. The output signal is up to $20V_{PP}$ imposing our upper limit in amplitude. The use of an amplifier to boost excitation and increase the maximum imposed strain, was considered, but not attempted as it could increase PZT hysteresis and adds harmonics to the signal. The signal path for conditioning and processing is the following: it first passes through a MMF M68 charge amplifier. Its basic function is to convert the charge generated at the transducer $Q(t)$ to voltage signal $V(t)$ achieving accurate stress measurement as described in section 2.3. By means of internal high-cut filters, the higher harmonics and noise are isolated and the signal is amplified 10 to 1000 times. The output is then fed both to our Tektronix TDS2000C oscilloscope and Stanford SR830 Lock-In Amplifier to be compared with the excitation signal (reference), in order to determine the amplitude and the phase advance of the stress response, yielding G^* and $\delta(t)$, respectively for a given measuring point. The RMS value (and not peak to peak) is taken as proportional to $|G^*|$, in a similar way to Miles device (Ferry, 1980). The Lock In amplifier multiplies the signal by a pure sinusoidal wave at the reference frequency. Sine waves of differing frequencies are orthogonal (when averaged), hence only the signal at the reference frequency will be processed and phase and magnitude will be extracted.

2.4.2.iii Loading and Plate Alignment

Loading requires caution not to break the plates, especially when the sample is stiff. The 3 holding screws have to be gradually tightened as the sample relaxes and the setting (fine threading) screws receive the pressure. For stiff melts, the sample was squeezed beforehand between two plates kept

apart with spacers. A uniform film just thicker than the gap was then loaded and the whole cell was placed in the oven at 45°C in order to relax faster as the holding screws were gradually tightened. Plate parallelism was set initially with spacers with the cell empty. Then a laser beam was reflected in both plates and directed to a screen (wall) via beam splitter. The two spots corresponding to each plate were matched by the “setting” screws, verifying parallelism with sufficient accuracy depending on the screen distance. Each surface produces a spot so this method was confusing with PZR1. Thus, in PRZ 2 the lower plate is not polished on one side (bottom) to diffuse the beam and the top was treated with antireflection “V” coating for the used laser wavelength (633nm). Both plates are optical grade BK7 glass with surface flatness grounded to $\lambda/4$. Relevant photographs and schematics are provided in appendix “A”.

2.4.3 Error analysis

The list of sources of errors for well-developed instruments like CRR can be extensive (Macosko 1994). Adding error sources intrinsic to the PZR will end-up in a discouraging list. Thus we will deal first with the latter and leave the rest to be dealt if/when considered important in the experimental data section.

2.4.3. i. EMI Noise

Noise can enter the measurement loop at any point. It is mainly electromagnetic interference (EMI) from external source that “contaminates” the response signal mainly by induction or electrostatic coupling. By analyzing the response signal with an empty cell –no sample loaded- with or without excitation, we have identified two categories. First and important it is the “crosstalk”, the EM coupling of the actuator and transducer element and their feed cables. Tests showed a response signal of few mV at the same frequency, as soon as an excitation was switched on, with the cell being empty. The strength on the early PZR1 designs could reach as much as 20 mv, similar with samples response. The new phase theta (θ) can be calculated from the equation below, which is derived from the mathematical superposition of two sinusoidal waveforms, with the same frequency, amplitude $V_{o_{in}}, V_{o_{out}}$ and phase difference δ . In our case $V_{o_{in}}$ and $V_{o_{out}}$ denote the input (excitation) and output (response) of the cell respectively.

$$\tan(\theta) = \frac{V_{o_{out}} \sin(\delta)}{V_{o_{in}} + V_{o_{out}} \cos(\delta)} \quad (2.13)$$

It is easily seen qualitatively, **that δ will decrease** with superposition. Filtering cannot improve the signal as the two frequencies are identical. Second are external sources of EMI derived noise i.e. electrical devices (i.g neon lights) or cables in adjacent labs, that we have no control of. Interference can enter the signal via power supply. Long-time averaging can mask such interferences exhibiting considerable errors in phase angle data. Very often these errors can be detected during measurement, for instance the phase angle for a specific data point decreases rapidly where other behavior (increase)

was expected. A slight change of the measured frequency may help in this case. In general remedy is based on:

- Shielding and proper grounding to reduce coupling. To this end, all signal cables are low-noise coaxial RG57u. Grounded loops should be avoided by setting some instrument / devices to “float”. Useful information can be found in (Morrison 1967). The trickiest part is to shield the cable terminals soldered on the piezo terminals. This has been achieved by means of copper tubes electrically connected to cable shielding for PZR1. In PZR2 shielding was successfully accomplished by the deep recess in the metal holders.
- Signal filtering and noise suppression. The simple approach is filtering. Fig 2.4.1 shows excitation and response signals as displayed in the oscilloscope during measurement. Although amplitude measurement is not severely affected, phase could be way off as zero crossing point is shifted significantly in time. The use of low-pass filter is the trivial remedy. They can attenuate noise, provided that its frequency is not close to the signal and the signal to noise ratio (SNR) is more than 0 db.
- Phase-sensitive detection by means of a lock-in amplifier. It is considered as “key” when phase angle needs to be measured. The signal frequency is known and fed-in as a reference signal allowing the device to lock-in allowing reasonable measurements even when the signal is weaker than the noise as has been described above. The procedure can be applied via a stand-alone device or PC with suitable software.
- Averaging helps to minimize only random and not systematic noise. Systematic noise i.e. 50Hz from power grid or switching power supplies cannot be removed.

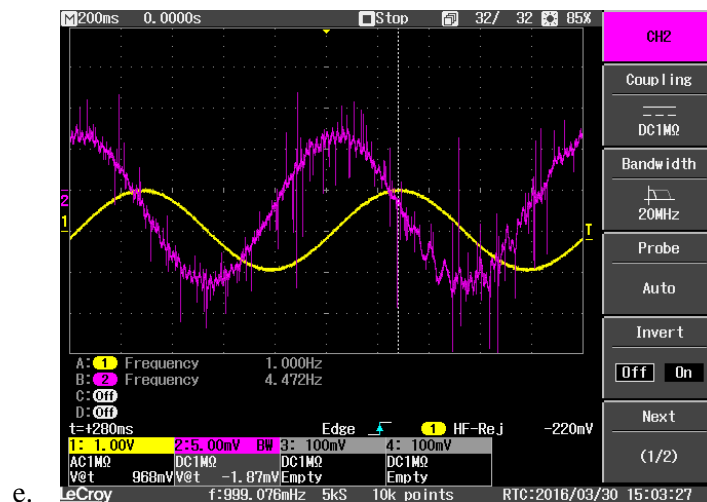


Figure 2.4.1: Noise in response signal (Chanel 2 shown in purple) introduces phase error. Frequency measurement by the instrument is also fooled displaying 4.47 Hz instead of 1 Hz which is the excitation signal (Chanel 1 shown in yellow)

2.4.3. ii. Acoustic Noise

Environmental vibrations can affect measurements. With Thorn Labs anti-vibration table, we did not witness any artifact in the PZR1. However when the more sensitive PZR2 was used, we

detected interference in weak signals; therefore, the system had to be isolated from external sounds. An alternative is the use of an acoustically isolated chamber to house the PZR, similar to Roth et al, however this will make the procedure of loading more complicated.

2.4.3.iii Mechanical Resonances

Resonances comprise the second important frequency-limiting factor, besides inertia. Simplicity in design really helps. Any **attachment** to the cell can resonate giving spurious measurements. PZR2 capable of larger displacement is more susceptible to resonances, a trade-off for sensitivity. As mentioned the MC was originally designed for compression mode thus lateral rigidity is not enough. PZR2 is stiffer than PZR1 as retaining bolts can be secured harder. **Dramatic** improvement was observed when the **excitation** holder plate was placed downward and secured firmly to the anti-vibrational metallic table. The top (measuring) plate was further supported by L-shaped metallic sections bolted to the table. Support was achieved by using set screws with rounded tips to avoid plate misalignment. Resonance was minimized but could not be avoided completely. By further increasing support pressure on the sensing plate, resonance point was shifted to higher frequencies. Fig 2.4.2 and 2.4.3 show PZR2 resonance signatures, commencing at 620 Hz for a colloidal glass and linear PBd solution, respectively.

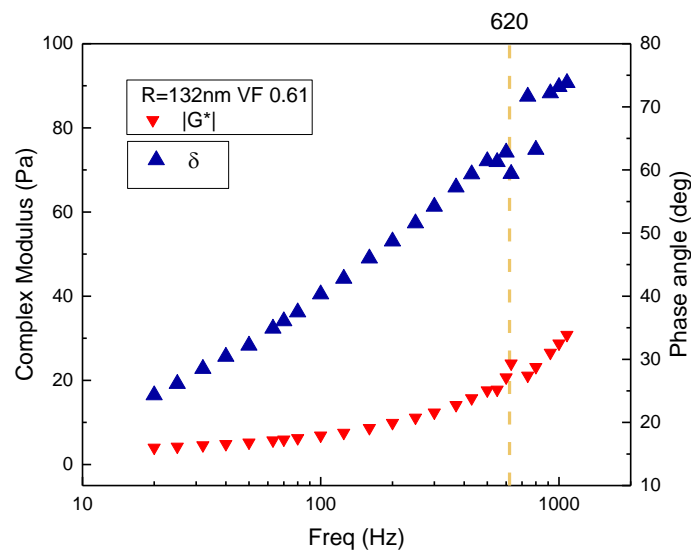


Figure 2.4.2 Amplitude and δ for ASM 330 hard sphere glass with particle radius $R=132$ nm at $\phi=0.61$ measured by PZR2. Resonance impact is profound at 620 Hz.

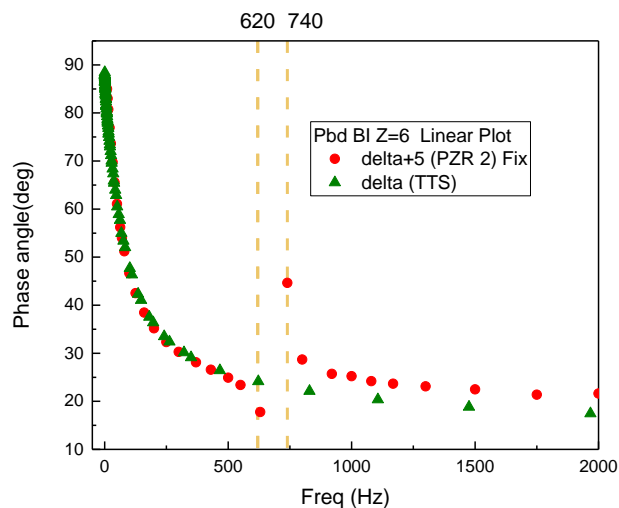


Figure 2.4.2 Phase angle (δ) for linear PBd solution Z6 measured by PZR2 against TTS data.

Chapter 3: Materials and Rheology

3.1 Brief Introduction to Polymers and Colloids.

The word Polymers derives from the combination of Greek words “Πολλά” “μέρη” meaning many parts. This is the simple definition of a macromolecule being the product of many smaller molecules, the monomers that do repeat with a specific pattern. In case of more than one type of repeat units we have a copolymer, which can be regular (block) or random. Chains can be linear or branched. Linear polymers present the simpler case regarding rheology and will be examined further in solution and melt state. Because of their structure, polymers exhibit rich rheological response extending several time scales from monomer to the entire chain. Mean-field modeling provides quantitative predictions. Experimentally the basic control parameters for a given system are temperature (T) and concentration (c).

A colloidal suspension is a system where mesoscopic discrete particles are suspended in a matrix. In this work, we study polymeric particles suspended in a Newtonian organic solvent. The mesoscopic scale (few nm to few μm) ensures that particles are small enough to diffuse (Brownian motion) as being “bombarded” randomly by solvent molecules due to thermal motion, and at the same time big enough for the continuum hypothesis to hold. Their size range can be within the resolution range of optical microscopy allowing their direct observation. The experiment control parameter is concentration, expressed in terms of volume fraction (ϕ). For monodisperse spheres, upon approaching $\phi \sim 0.58$, we observe a dramatic slowing-down of long-time (or large-scale) dynamics, with a strong ϕ dependence, which leads to a non-ergodic transition, from a liquid to a kinetically

arrested glassy state, termed “glass transition”. Our lack of understanding the glass transition upon first principles, is reflected in the following phenomenological definitions:

- a. when the viscosity is 10^{15} times that of water, simply because viscosities that are larger become problematic to measure (Weeks, Crocker et al. 2000)
- b. when the relaxation time approaches a range 1–1000s, the corresponding range of temperatures or volume fractions defines the glass transition region (McKenna 2006)

3.1.1 Diffusion in the Dilute Limit

Stochastic motion in colloids is due to thermal forces, as particles are being hit by solvent molecules. This “Brownian motion” is reflected in the material’s rheological response (relaxation). Using the Stokes-Einstein-Sutherland equation one can calculate the diffusion coefficient of a **single** non-interacting spherical particle in the dilute limit (Mewis and Wagner 2012):

$$D_o = \frac{k_B T}{6\pi\eta R_H} \quad (3.1)$$

The nominator denotes the “driving” energy (thermal energy) and the denominator the resisting macroscopic “force” due to friction of the particles surface within the medium. Once the diffusion coefficient is known, the characteristic time (t_b) can be extracted using simplified form (Fick’s law of diffusion) :

$$6D_o t = \frac{R^2}{\tau_b} \quad (3.2)$$

where τ_b denotes the time for a particle to diffuse a distance equal to its radius in infinite dilution and sets a fundamental time-scale. The important message of equation (3.1) is that solvent viscosity (η), a macro-rheological property, can be extracted simply by observing the motion of a dispersed particle.

3.1.2 Colloidal Micromechanics and Softness of Hard Spheres

The mechanical response reflects the interplay of particle microstructure (interaction potential) and hydrodynamics. Particle configuration is determined by entropy that dominates the free energy in the absence of enthalpic interactions (long range repulsions or attractions) in dense suspensions. Brownian motion will gradually drive the particles toward an entropic maximum. The coupling with hydrodynamics results in non-negligible particle-particle and particle-solvent forces:

- Brownian Forces drive self-diffusion. Due to their thermal origin they scale with temperature $T : F_B = k_B T / R$
- Stokes drag competes against particle movement in the solvent. Friction drag force is defined as $F_{sd} = 6\pi n_{sol} R v$, in laminar flow under boundary no slip conditions and R is particle radius, v is its relative velocity to the solvent and η_{sol} is viscosity of the solvent.

- Attractions due to ubiquitous dispersion (van der Waals) forces. Their origin is the fluctuating molecular dipole interactions. The relevant pair potential is approximated by $U_A = \frac{-AR}{12x}$ where A is the Hamaker constant, a material property representing attractive interactions in vacuum and x is interparticle distance. Since colloids (in our case) are suspended in a solvent the effective Hamaker constant can be defined $A = (\sqrt{A_{par}} - \sqrt{A_{solv}})$. Obviously, particles and solvent with dissimilar chemistry, indicated by refractive index mismatch, should have attractions that may lead to aggregation. In our case to achieve nearly hard sphere interactions we use sterically stabilized poly-methylmethacrylate (PMMA) particles, where the steric stabilization is achieved by a thin layer (10nm) of poly-hydroxy-stearic acid (PHSA). Moreover we minimize vdW attractions by suspending the PMMA particles in **squalene** with reasonable refractive index matching.
- Repulsion due to osmotic and other forces. In our case repulsion originates from two sources. Steric Stabilization and hard-sphere potential reaching infinity when ideally particles touch. Steric stabilization is accomplished by “grafting to” a thin “hairy” layer of PSHA at the particle surface. Layer thickness is around 10nm inducing short-range repulsions represents a model hard sphere system (Pusey 1991) (Royall, Poon et al. 2013). Deviations from ideality are expected especially when interparticle distance reduces to nano-metric scale and PSHA layers inter-digitate. Repulsion “kicks in” at 15 to 8 nm and is maximized at 6.2 nm where inter-digitation is maximum (Bryant, Williams et al. 2002). A schematic illustration of interparticle potential is depicted in the figure below:

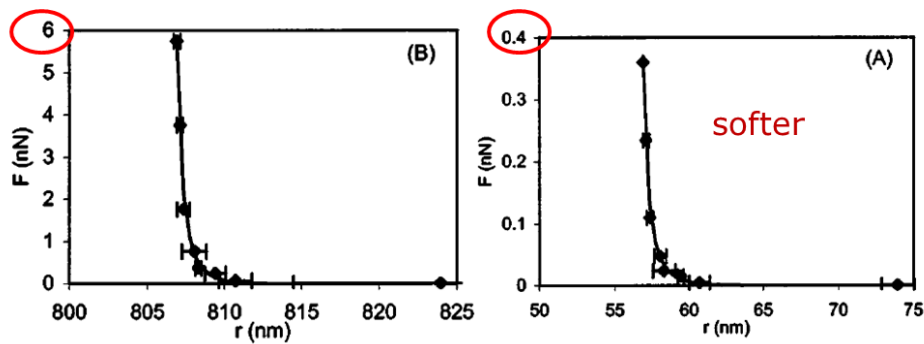


Figure 3.1.1 Repulsive force for hard ($R=800\text{nm}$) and less hard ($R=50\text{nm}$) sterically stabilized spheres. Points represent experimental data, and the lines calculations (Bryant et al, 2002)

- Hydrodynamic interactions mediated by solvent between particles. Their motion disturbs the flow field, which in turn sets-in / affects the motion of other particles. The fundamental mechanism is momentum exchange between particles and solvent molecules. Interactions could be long- or short-ranged and their theoretical study is definitely non-trivial. The resulting force is

$$F_h = \frac{6\pi\eta U}{(x-(R_1+R_2))} \frac{R_1^2 R_2^2}{(R_1+R_2)^2} \quad (3.3)$$

where $(x - (R_1 + R_2))$ is the surface-interparticle distance. The equation holds within the lubrication limit where the center-to-center distance $x \ll 2(R_1 + R_2)$ (Mewis and Wagner 2012). Obviously, the force diverges to infinity when particles touch, hence hydrodynamic interactions become dominant when particles are concentrated or come close under perturbations such as shear. At this nanoscale level interparticle distance, surface roughness becomes important.

Considering the above forces of different nature, it is obvious that is far from trivial to calculate the full interactions with a 3D many-body model. As concentration increases, the response is strongly dependent on particle configuration.

3.1.3 Crystallization of Hard Spheres

Based on simulations and experimental observations, monodispersed hard-sphere suspensions crystallize. A polydispersity of around 7% or more suppresses crystallization and leads to amorphous solidification. The non-trivial effect of polydispersity on glass transition and the importance of particle size distribution (PSD) has been extensively studied (Zaccarelli, Liddle et al. 2015). Hence, we chose our PMMA spheres samples to have a polydispersity of around 10% to avoid crystallization.

3.1.4 Colloidal Repulsive Glass

The importance of concentrated nearly hard-sphere systems in rheological studies is profound considering that it is one of the simplest mesoscopic systems exhibiting glass transition. They are used as a basic model and reference point for other more complicated soft matter systems, such as multiarm stars or soft micelles and emulsions, where various dynamic relaxation modes present similarities due to analogous topology (Vlassopoulos 2016) but also a model system to study the more general problem of glass transition. As the suspension becomes more crowded beyond a critical volume fraction (0.58) the dynamics slows down dramatically with strong ϕ dependence. Ergodicity brakes down and the system's evolution towards equilibrium (crystal) is halted due to kinetic constraints or becomes path (initial conditions)-dependent (for example under shear it might crystallize) (Koumakis, Schofield et al. 2008). Note that, as mentioned above these are nearly hard spheres, i.e., repulsive interactions dominates, hence the term repulsive glass.

3.1.5 Colloidal Attractive Glass and Other Colloidal Glass Formers

Hard sphere potential can be significantly altered by the addition of a non-absorbing polymer of suitable size (R_g). Depletion forces of osmotic origin will cause interparticle short-range attraction. This leads to a departure from the well-established cage picture, with a behavior varying depending on the strength of the attractive potential. At low attraction $U \approx k_B T$ a weak clustering is observed which increases the local free volume and melts the glass (Pham, Egelhaaf et al. 2004) (van de Laar,

Higler et al. 2016). Upon increasing attraction further, physical bonds between neighboring particles form, whose lifetime grows with attraction strength. This causes a re-entrance into a bonding-dominated glassy state whose properties are different from those of a hard sphere glass. Re-entrant glass is only expected for short-range attraction, consequently the range of the potential is as important as its strength. This is the case of an attractive glass.

Beyond hard spheres one can find also soft deformable colloids with particles like microgels, stars and micelles, where softness can be induced by long polymeric chains and interpenetration is important by a cross-linked outer layer network which may induce deformability. The effective volume fraction is the control parameter and is calculated based on the single particle hydrodynamic size (Vlassopoulos and Cloitre 2014). The list of various colloidal glassy systems is endless. An indication of this variety and diversity is the example of laponite nanometer-sized colloidal clay platelets that become non-ergodic (kinematically arrested) at $\phi_g \approx 0.02$. However this particular system is extreme due to its complexity.

3.1.6 Self Diffusion and Time scales in the Glassy State

Caging results in two distinctive diffusive mechanisms, the long-time, related to the out-of-cage motion, and the short-time, related to the in-cage one. Particle motion can be observed directly by confocal microscopy (Weeks, Crocker et al. 2000) and can be portrayed by the mean squared displacement (MSD) after time t i.e. $\langle \Delta r^2(t) \rangle = \langle |r(t) - r(0)|^2 \rangle$ where $r(t)$ denotes position coordinate at time t and the brackets averaging over all observed particle trajectories (ensemble). Particle dynamics and caging have also been studied extensively by Dynamic Light Scattering (DLS) which probes the intermediate scattering function (ISF) decay (van Megen and Schope, 2017)(Weeks 2017). The ISF decay characterizes particle spontaneous fluctuation about equilibrium that can be related to the systems response to a weak (within linear regime) mechanical perturbation, via the fluctuation dissipation theorem (Kubo 1966). The idea is that the decay of a fluctuation is independent of its origin i.e. spontaneous due to thermal noise or induced by a small applied force.

Below, we discuss time scales which reflect the particular microstructure. Particle velocity fluctuates on a Brownian time (τ_B) scale of the order of $\tau_B = m/6\pi\eta R$ where m is particle mass, R its radius, and η the zero shear viscosity of the solvent (Dhont 1996). This time corresponds to particle momentum relaxation in other words is the time required for hydrodynamic interactions to reach steady state (Wagner 1993). It sets the short time limit for the period of oscillation in order for the statistical (Smoluchowski) description of the dynamics to be valid and particle inertia to be neglected (Beenakker 1984, Lionberger and Russel 1994). In extremely fast snapshots, just above solvent picosecond relaxation times, not easily accessible experimentally, a particle moves ballistically with $\langle \Delta r^2(t) \rangle \sim t^2$ (Pusey 2011). As observation time increases ($t \gg \tau_B$) the under consideration particle termed tracer, sustains numerous collisions slowing down to an average speed, exhibiting Fickian

diffusion where $\langle \Delta r^2(t) \rangle \sim t$. This is the Brownian regime where the tracer should exhibit uncorrelated step motion as a result of random collisions although it has been shown that these steps display a non-Gaussian distribution in very dense and heterogeneous media (Guan, Wang et al. 2014). In crowded systems (colloidal glasses) and longer times, particles become strongly coupled hence MSD is influenced as motion is hindered by direct and hydrodynamic interactions, exhibiting sub-diffusive behavior (Pusey 2008) (Polanowski and Sikorski 2017). This is indicative of the systems memory (Weeks and Weitz 2002) and is observed at times longer than τ_β where the tracer starts to feel its cage whereas at times $t > \tau_\alpha$ longer times it escapes its “phantom” confinement as cooperative motion forms and annihilates cages simultaneously. It should be mentioned that the ideal Mode Coupling Theory (MCT) glass transition picture, predicts the “alpha” relaxation time to diverge at ϕ_g (out-of-cage motion is frozen) whereas other theories i.e. DLT as discussed below, predict this behavior at maximum packing fraction ϕ_{\max} or ϕ_{rcp} . As particles interact and slowdown in crowded systems, the dilute regime self-diffusion coefficient D_0 , should be turned into a D_S at short times and a D_L at long times, i.e. the short- and long-time self-diffusion coefficients respectively. From this perspective and considering the ideal MCT picture, $D_s(\phi)$ and $D_L(\phi)$ converge to zero at ϕ_{\max} and ϕ_g respectively. Since our study is related to high volume fractions we shall attempt at linking the results (time scales) to the different ϕ dependence of D_s and D_L (see fig 3.1.2).

Both MCT and Dynamic Localization Theory (DLT) predict a cross-over volume fraction where particles are localized by the cage. Contrary to the ideal (naïve) MCT, DLT relates the cage boundaries to entropic barriers that confine the particles for times smaller than hopping ones. Thermally activated hopping may eventually lead to escape of a few particles from the barrier, within the observation time (Saltzman and Schweizer 2006). Out-of-cage diffusion is predicted to freeze only well above glass transition at ϕ_{\max} . More on this model will be discussed in section 3.3 and Chapter 5.

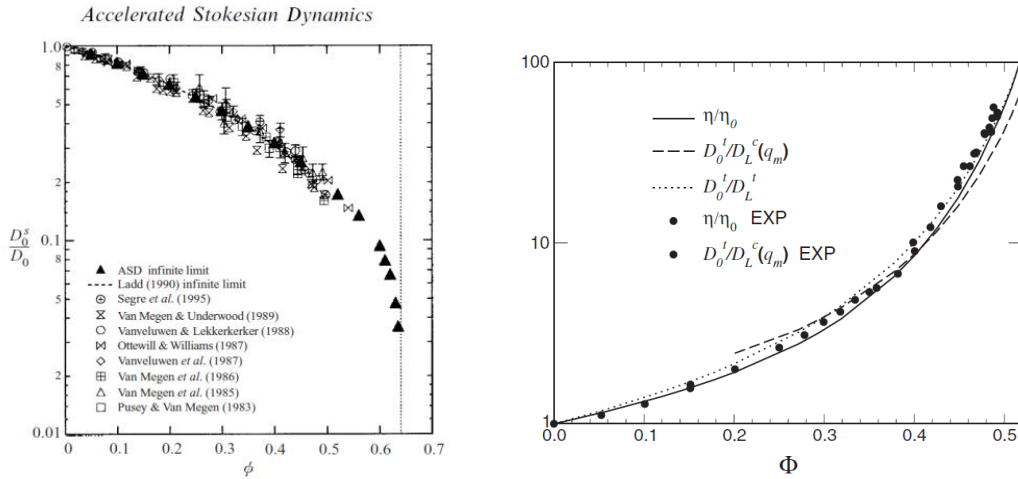


Figure 3.1.2 Short-time self diffusion coefficient decreases at higher volume fractions as cage becomes tighter. Left: D_s/D_0 vs ϕ dependence in semi-log plot for (From Sierou and Brady, 2001) Right: Similar for the reciprocal quantity D_0/D_s (Nagele, 2013).

3.2 Linear Viscoelasticity of Linear Polymer Chains.

Linear polymers have rich and interesting rheological features, being thermo-rheologically simple systems hence representing the ideal candidate for evaluating PZR’s performance. For molecular weights above the entanglement threshold (M_e) chains are topologically constrained due to entanglements, constituting a physical network, where junctions are constantly annihilated and created, due to the one-dimensional reptational (curvilinear) motion, within their topological tube.

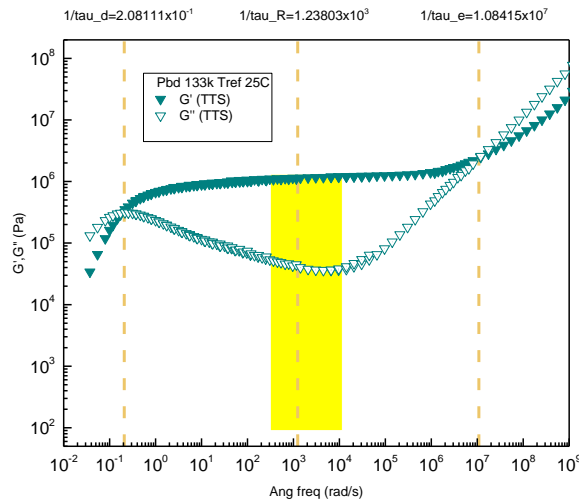


Figure 3.2.1 Mastercurve of Linear PBd melt at Tref: 25C°. Yellow area marks the usable parametric envelope of PZRI (Data taken by. Salvatore. Costanzo)

Figure 3.2.1 illustrates the so-called master curve of linear polybutadiene with $M_w = 133\text{kg/mol}$. It was constructed by applying (TTS). Frequency spans many decades, something not feasible with conventional rheometry. As observation times become shorter, the first crossover marks the transition time τ_d from terminal flow to a solid like “rubbery plateau” corresponding to relaxation

of chain segments between entanglements. In this time region, G' is frequency-independent and its value, the plateau modulus, scales inversely with M_e , the later been a fundamental scaling parameter in the tube model:

$$G_N^0 = \frac{4}{5} \rho RT / M_e \quad (3.4)$$

Reptation theory was later enriched with non-reptative mode like contour length fluctuation (CLF) due to the dangling free chain ends facing less constraints than tube internal monomers and constraint release (CR) that readjusts tube diameter over time. LVE data for polybutadiene, our “favor candidate”, have been found to agree well with this enriched theory (Likhtman and McLeish 2002). The number of entanglements per molecule is $Z = M/M_e$, equal to the number of tube segments per molecule although linking M_e to G_N^0 is more complicated (Larson, Sridhar et al. 2003). By further decreasing the time window other relaxation mechanisms emerge marked by τ_R , the Rouse time of the chain within its tube, τ_e the Rouse time of an entanglement segment and τ_o , not accessible here, the monomeric time that marks the transition towards the glassy plateau, where chain movement is “frozen”.

In search for the “favored candidate” we ruled out PBd133k, being too stiff for our cell and displaying a strong solid-like behavior, with very weak viscous dynamic component (δ varies from 2° to 3.4°). It stands at the edge of PZR1 parametric envelope marked in yellow in fig 3.2.1 and is very sensitive to δ error. In order to tune dynamics we focus on the strong power-law dependence of τ_d with molecular weight $\tau_d \propto M^{3.4}$ for $M > M_c$. M_c stands for a critical molecular weight threshold being around 5900 for PBd ($M_c \cong 2 \cdot M_e$). Now by using the above scaling for time and plateau modulus we found a more suitable sample, PBd 24k with $Z \sim 12$ entanglements per chain. Concentrated solutions with average molecular mass $M_{(\varphi)} > M_c$ were also used to further tune dynamics by varying Z based on similarities of their dynamic scaling laws (Baumgärtel and Willenbacher 1996). The molecular weight between entanglements $M_{e(\varphi)}$ scales with volume fraction φ as:

$$M_{e(\varphi)} = M_{e(melt)} \varphi^{-\alpha} \quad (3.5)$$

where α is the dilution exponent with a suggested value of 1 (Graessley 2008) (Huang et al 2013). Based on this Pbd, solutions with $Z \sim 9, 6$ and 3 were prepared.

The Time Temperature Superposition (TTS) method is feasible when relaxation mechanisms of a fluid exhibit the same temperature dependence. Time temperature shifting for time domain modulus can be expressed as:

$$G(t, T) = G(a_T t, T_{ref}) \quad (3.6)$$

This defines the “class” of thermo-rheological simple materials (Schwarzl and Staverman 1952). Dynamic data at different temperatures can also be shifted vertically (moduli) and horizontally

(frequency) in order to obtain the master curves of the material for a wide frequency range at a chosen reference temperature T_{ref} . The so-called horizontal shift factor a_T can be calculated from Williams, Landel, Ferry (WLF) equation :

$$\log a_T = \frac{-C_1(T-T_{ref})}{C_2+(T-T_{ref})} \quad (3.7)$$

where C_1, C_2 are quasi-universal values similar for many polymers. Likewise moduli has to be shifted with the vertical factor b_T , reflecting the temperature variation of density (Dealy and Plazek 2009). Consequently shift factors are functions of temperature. They are often fitted to derive the WLF behavior, over a wide range of temperatures, however the validity of the latter is often questioned. Nevertheless, TTS is the best available tool to access so huge frequency range in many materials such as linear polymers and branched polymers, provided no phase change takes place at the usable temperature range.

3.3 Linear Viscoelasticity of Colloidal HS Glasses

Ideally, a typical dynamic frequency sweep (DFS) curve of a glass will look like figure 3.3.1 (left) where the two moduli crossovers corresponding to $\tau_{ca} = 1/\omega_{ca}$ and $\tau_{c\beta} = 1/\omega_{c\beta}$ respectively, mark three regimes

- a. At the low end (long times) structural rearrangements result in a mainly viscous response. Brownian motion prevails contributing to loss modulus. Experimentally this is very difficult regime for oscillatory tests and spurious measurements may result due to microstructure instabilities. This is why it is not well captured in the plot. Compliance data for discrete times, taken in creep tests, can be converted to dynamic moduli (Evans, Tassieri et al. 2009) thus expanding the low-frequency spectrum. But this is again not trivial (Siebenbürger, Ballauff et al. 2012).
- b. In the intermediate spectrum the system demonstrates its real glassy character with a rubbery-like plateau. Energy storage increases with increasing frequency as the perturbed suspension structure is unable to relax during oscillation. The plateau is determined at the viscous component minima.
- c. Interestingly, the upper end the system displays again a liquid behavior. At short observation times the particle seems unrestricted by neighbors a “virtual” transition from solid to liquid, marked by the second crossover.

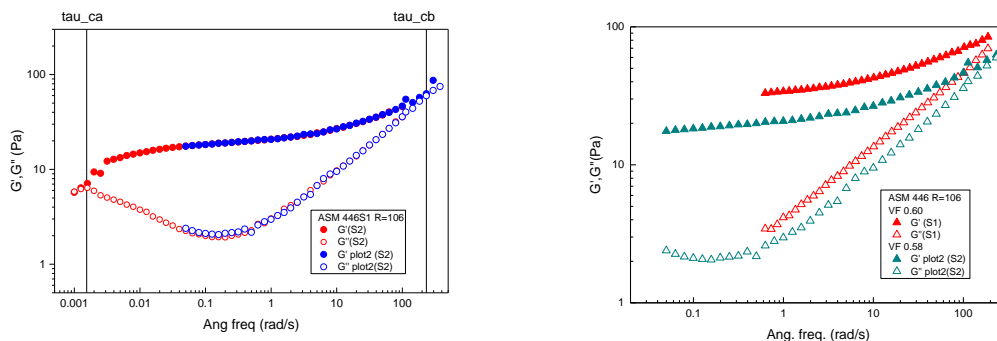


Figure 2.3.1 Dynamic moduli data taken with MCR 702 for $R=106$ nm colloidal glass Left: full frequency scan approaching instrument limits Right: comparison between different volume fractions 0.60(S1) (red) and 0.58 (S2)(blue).

A broad DFS spectrum for a small-sphere glass $\phi=0,58$, obtained with CRR (MCR702), is shown in fig 3.3.1 left. The right plot depicts DFS data for different ϕ where the denser glass (red symbols) exhibits larger moduli values and faster beta relaxation time as the cage becomes tighter. On the contrary, out-of-cage motion needs more time to be captured, hence both crossover times τ_{ca} and $\tau_{c\beta}$ have been pushed outside the instrument's frequency limits.

3.3.1 Scaling Laws at Short Times and High Volume Fractions

Our samples were chosen to be stiff in order to provide sufficiently strong signal for the less sensitive PZR1, and this led to very dense and fragile glasses. Small observation times result in hydrodynamic interactions (HI) being more dominant and the “in cage” diffusion to dramatically slow down, portrayed by a significant drop of D_s (fig 3.1.2). Consequently, short-time dynamics are affected significantly while long-time dynamics are less affected by HI (Thorneywork, Rozas et al. 2015). Theory and experiments suggest that after the high frequency crossover the loss modulus should vary linearly with frequency, indicative of a constant dynamic viscosity (n'_∞) as a result of dominant hydrodynamic contribution to the viscosity (Fritz, Pechhold et al. 2003). On the contrary, the origin of storage modulus is different and is strongly affected by the deformability of the stabilizing layer (Mewis and Haene 1993) thus it shows different limiting behavior. Bare spheres exhibit a plateau, but the more complicated sterically stabilized ones divert, following weak power laws (Willenbacher and Oelschlaeger 2007). We suggest that HF rheology provides the **magnification lens** of particle surface texture or roughness.

The scaling laws for HS are based on the principle that elasticity is set by temperature ($k_B T$) (Mason and Weitz 1995) and as such, dynamic moduli should collapse into a single curve when normalized by thermal energy per volume and reduced time (Koumakis PHD thesis, 2011). In dense regimes and at sort times this scaling is expected to deviate for hairy particles due to hairy layer inter - digitation and possibly due to heterogeneities (Berthier, Biroli et al. 2011). Additionally, at short times the solvent is squeezed out generating lubrication forces that contribute to a more complicated

behavior (Elliott and Russel 1998, Swan and Zia 2013). In a more generalized view consistent with the above, jamming contribution only affects the stresses at large Peclet numbers where PMMA colloids deviate from HS behavior (Ikeda, Berthier et al. 2013). Peclet number simply scales with frequency but quantifying self diffusion coefficient and consequently Pe for near-jamming regime is quite challenging. Scaling data with D_0 removes only the trivial Stokes flow hydrodynamic effects associated with the movement of a single particle in a solvent. Dynamic viscosity η' is related to G'' dependence on frequency. Its limiting value is important as it reflects the energy dissipated by a flow associated with the equilibrium arrangement of particles (Lionberger and Russel 2000). Rheology definitely becomes more challenging at the highest concentrations (Russel, Wagner et al. 2013) where effective volume fraction is needed for scaling near/hard spheres. Furthermore strongly anomalous and aging dynamics have been observed for PMMA particles by X Ray Photon Correlation Spectroscopy (XPCS) (Kwasniewski, Fluerau et al. 2014). The group supports that the **departure from MCT** predicted long- and short-time dynamics happens at lower volume fractions than originally believed. They also suggest a **hyperdiffusive** behavior at ϕ around 0.61 as a result of faster relaxation processes due to distributed stress, despite the sample been at quiescent state. MCT is a nearly first-principles approach based on collective density fluctuations and relates forces, structure and slow relaxation, but was developed to describe the picture in the vicinity of glass transition. Classic MCT has been characterized as “naïve” based on the fact that glass transition is formally a mathematical singularity, where the relaxation time (and other quantities) diverge due to the theory’s neglect of activated processes. Dynamic localization theory (DLT), an extension of MCT, removes the classical cage picture and considers instead, a pseudo potential that will generate the same particle transport properties. This results in two forces a) a finite one from the immediate neighbors, which the tracer can overcome after sufficient time, by thermally activated hopping b) an elastic one from distant neighbors. This picture allows MCT singularities to be removed up to RCP and seems to describe system’s behavior (i.e. viscosity, long-time self diffusion coefficient and modulus) better at higher ϕ . (Jiang and Zukoski 2014) (Schweizer and Saltzman 2003) (Koumakis, Schofield et al. 2008). The virtual energy barriers, *termed dynamic potentials*, represent entropic traps that particles have to overcome, and characterize the rate at which the system achieves equilibrium thus arguing that the suspension remains at equilibrium approaching random close packing. Dynamical slowing-down is considered an abrupt but continuous process with increasing volume fraction. Short-time self-diffusion is also correlated with the restricted motion related to localization length (r_{Loc}). The latter can be calculated by considering the governing micro-mechanical forces within the entropic trap model (Jiang and Zukoski 2014) and (Mirigian and Schweizer 2014). We will utilize DLT-based scaling laws to analyze data in Chapter 5.

3.3.2 *Criteria for onset of Non Linearity*

During this work concerns have been raised about possible onset of nonlinearity due to the simple concept that high frequency oscillating particles are in close proximity and hydrodynamic interactions could affect their microstructure (Swan and Zia 2013). We define linear response or linear relaxation as the regime where the time or the frequency dependence of the relaxation process does not depend on the size of the imposed perturbation, in our case is strain amplitude independent. The LVE limit can be experimentally tested via amplitude sweeps, performed with MCR 702 or PZR at fixed frequencies and is confirmed to vary around 0.8 % at 10 Hz. Theoretically the onset of nonlinearity for HS colloids requires either strain or strain rate to overcome a critical threshold, depending on the nature of the deformation (Kumar et al ,2016). Our strain of 0.001 % is extremely small compared to 0.8 % typically observed, but strain rate increases with frequency. On the other hand, the strain limit for linearity decreases with increasing particle size and volume fraction but increases with frequency (D Haene, Phd thesis, 1992). However, critical strain for other phenomena that cause deviation from the expected HS behavior, seem to decrease with an increase in frequency reaching a minimum, possibly due to particle boundary slip, within the high-frequency regime (Lee and Wagner 2003),(Chang, Friedrich et al. 2010). Mesoscopically, at high ϕ , activated processes are extremely slow thus the shear rate required to achieve linear response can be exponentially small and is governed by the activation barrier (Russel, Wagner et al. 2013). In our tests we have not detected nonlinear behavior. Although this may be undetectable in our case, we believe that the frequency dependence of critical strain at elevated frequencies, should be further studied.

3.3.3 *Impact of Wall Slip on Colloidal Glass in Oscillatory Tests*

Slip has been extensively studied in steady shear flows of polymers (Hatzikiriakos 2015, Chatzigiannakis, Ebrahimi et al. 2016) and colloids (Cloitre and Bonnecaze 2017). In oscillatory tests, it is of major concern in large amplitudes (LAOS)(Yang and Yu 2017) (Yang et al ,2017). However, the mechanism of slip is very different in colloids, where a particle depletion boundary layer is formed and slip dominates at high volume fractions when sample plates are smooth(Ballesta, Petekidis et al. 2012) and at elevated frequencies (Mewis and Wagner 2012). Our tests fulfill all above criteria, thus its impact on our measurements must be considered.

Under slip, the frequency-decomposed stress (Fourier components) signal can include even harmonics in addition to the odd ones characterizing the nonlinear regime. Response can become more complicated with quasi-periodic or chaotic patterns studied by implementing attractors (introduced by Lorentz in Chaos theory to study weather patterns) (Adrian and Giacomin 1992). This means that it may be easy to suspect but challenging to prove, by just analyzing the rheological signature. On the other hand, by measuring in different gaps one can check for slip but cannot always extract bulk fluid properties using two-gap data as can be done for steady shear (Yoshimura and

Prud'homme 1988). The latter author, modeled slip of an arbitrary fluid with constant and varying slip layer fluidity, concluding that in oscillatory tests the presence of slip **enhances $\tan\delta$** , hence the sample appears to be less elastic. We shall use this result in our data analysis.

3.3.4 Dimensionless Quantities for Oscillatory Shear

In oscillatory tests, the Deborah number (De) - often termed Peclet-omega in colloids quantitatively describes the ratio of Brownian over perturbation time scale:

$$De = \omega \cdot t_{ch} = a^2 \cdot \omega / D_s(\omega) \quad (3.8)$$

where t_{ch} is the characteristic particle time. On the other hand, the Weissenberg number: $Wi = \dot{\gamma}_o \cdot t_{ch} = \omega \cdot \gamma_o \cdot t_{ch} = \gamma_o \cdot De$, where $\dot{\gamma}_o$ is the maximum shear rate amplitude during oscillation. We could say that De and Wi are both dimensionless time-scale perturbation indexes that include or do not include strain amplitude respectively. Consequently, Weissenberg number indicates the perturbation magnitude with respect to the equilibrium limit, as it contains strain amplitude and rate. However, the maximum values for strain and strain rate are obtained at different times (sin(t) and cos(t) functions) with the difference been equal to a quarter of a period.

Chapter 4: Calibration and Validation

Calibration is the setting or correcting of a measuring device by adjusting it to conform to a well-known parametric value(s). The strict definition in metrology is more complicated. In simple terms, we need a test sample, a rheologically well-characterized material (standard) that we can measure and compare our results to known values. The two true sensing parameters here are time corresponding to phase (δ) and stress corresponding to magnitude ($|G^*|$). Consequently, both time and stress measuring loops must be calibrated and validated.

4.1 Calibration I : Electronic Error Compensation

Our charge amplifier has integrated filters necessary to remove frequency components related to noise and harmonics. Although the lock-in amplifier can isolate the response related signal, too much noise would overdrive the charge amplifier inducing distortion. Hence, we use high-cut (low-pass) filters with various cut-off frequencies 1k,10k and 20 kHz. Filters induce phase shift and gain change that varies with filter setting (cut-off frequency) and measuring point (frequency). We have found that the gain is not significantly affected unless we exceed the 50% of the nominal cut-off frequency limit whereas at cut-off frequency the signal is attenuated by 3db, as shown in figure 4.1.1 (left). On the contrary the phase is shifted significantly as we operate at frequencies exceeding just 10% of the cut-off nominal value, as depicted in the Bode plot of the same figure (right), providing the first clue that phase angle (δ) measurements need more attention.

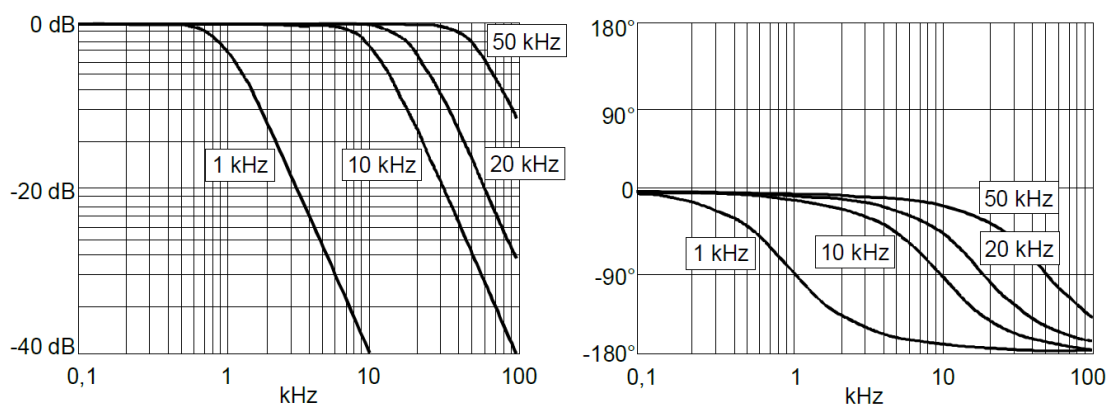


Figure 4.1.3 Frequency response (Bode) plot of MMF M68 charge amplifier (taken from device manual).

To compensate for this error, we need a more accurate plot thus we have performed measurements by feeding the M68 charge amplifier with a sinusoidal input directly from the signal generator. In the schematic below (fig 4.1.2), the capacitor C simulates the Piezo impedance (28 nf for PZR1). An

ohmic attenuator is also used to prevent amplifier overload. The output signal is then compared with the input and phase, and the gain is reported for discrete frequencies, a DFS analogue.

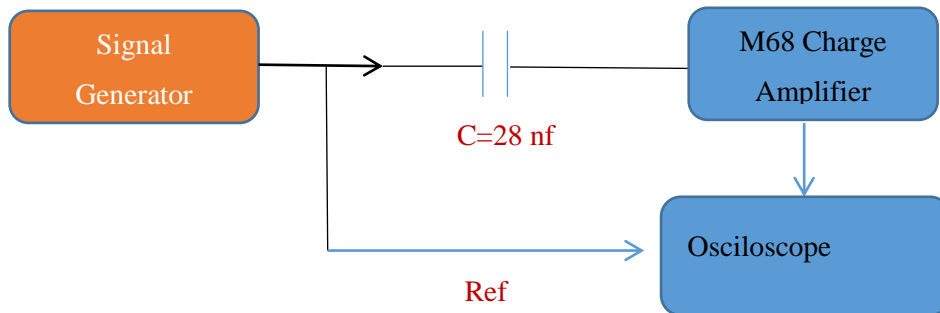


Figure 4.1.2 Test setup schematic. Capacitor C emulates piezo capacitance

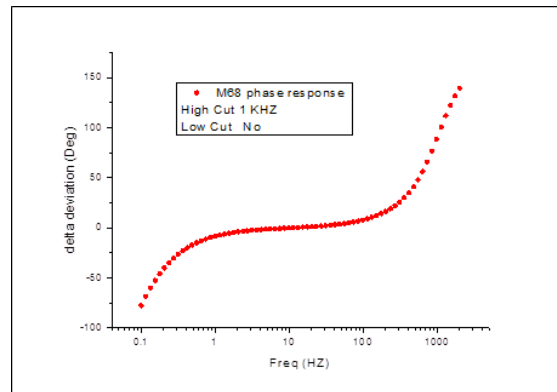


Figure 4.1.3 Phase shift (error) induced by our M68 charge amplifier measured for 28nf piezo capacitance.

Measurements were performed at discrete frequencies for different filter settings: 1k, 10k, 20k Hertz for high-cut and 0.3 Hertz for the low-cut. Figure 4.1.3 shows phase response for 1 kHz high-cut filter, where the phase shift exceeds 90° around the cut-off threshold. Being more convenient in practice, a phase response matrix was constructed for each filter configuration and Piezo capacitance. An example is shown in the table below. Data in the 2nd and 3rd column indicate phase correction factor for each discrete frequency tested and filter setting, thus it is more accurate and convenient to measure at these fixed points. However, via interpolation any frequency point correction factor can be calculated in suitable steps to resemble any logarithmic or linear increment.

Frequency	Phase angle correction factor	
	High-cut: 1kHz Low-cut: Not applicable	High-cut: 10 kHz Low-cut: Not applicable
10	0.0	-0.7
12	0.3	-0.6
15	0.7	-0.4
20	1.2	-0.2
25	1.7	0.0
32	2.4	0.1
40	3.1	0.2
50	3.9	0.4
63	5.0	0.5
70	5.6	0.6
80	6.4	0.7
100	8.1	1.0
125	10.1	1.2
160	13.1	1.6
200	16.4	2.0
250	20.6	2.5
300	25.0	3.0
370	31.2	3.7
430	36.7	4.2
500	43.3	4.9
550	48.1	5.4
630	55.9	6.2
740	66.7	7.2
800	72.5	7.8
920	83.7	9.0
1000	90.6	9.7
1080	97.0	10.5
1168	103.5	11.4

Table 4.1 Correction factors for 1kHz High-cut filter. Non shaded cells indicate the applicable correction factors for each frequency point and filter setting.

During measurements the noise is monitored and filters as set accordingly, in order to keep cut-off frequency as far as possible from the measured one. Usually a filter of 1kHz is necessary up to 125 Hz range. Then 10kHz filter is used. Data at 125 Hz are measured with both filters and their agreement after correction, helps identifying possible artifacts (consistency check).

4.2 Calibration II: PDMS

Having completed the previous step, Calibration II should standardize the whole setup in terms of phase and magnitude accuracy. For commercial rotational rheometers two basic calibration methods can be implemented by the user. The first calibrates the instrument by performing a steady shear test with a PDMS oil of known viscosity (η_o). Obviously this calibrates **only** the stress magnitude measuring loop, that corresponds to $|G^*|$ in DFS tests, as no time (δ) measurement is involved. Steady shear tests cannot be performed with our PZR. The second involves a solid (metal) and a “Newtonian” fluid standard in order to perform oscillatory tests and adjust phase angle measuring loop. Attaching a metal strip between our glass plates is not practically easy and on the other hand it is impossible to find a “viscous” PDMS standard that behaves as Newtonian up to 2 kHz. Viscosity calibration standards have been designed for steady measurements. Their polymeric nature results in relaxation mechanisms that will induce non-Newtonian behavior in oscillatory tests.

Our approach for Calibration II is to characterize a fully viscoelastic sample with a commercial rotational rheometer (CRR). We chose MCR 702 operated in SMT configuration, with plate-plate geometry (parallel disks) better suited for higher frequencies (Läuger and Stettin 2016). Then we compared the dynamic moduli data taken with MCR 702 against the PZR1 ones at the overlapping frequency region of 10 to 20 Hertz. Our “favored” sample should provide strong enough response to be detected by the PZR and rich phase variance (moduli crossover within the PZR frequency range) to adequately test the phase sensing loop. AK 1000000, a viscous silicon oil ($\eta=1000$ Pa s) used in drilling industry was selected. Dynamic moduli crossover at 123 rad/s falls within the MCR702 and PZR1 overlap regime. Lower viscosity samples were also tested ($\eta=100$ and 12.5 Pa s) in order to determine instruments sensitivity. As mentioned we consider phase errors more difficult to tackle, thus at this stage we focused on the phase measurements Fig 4.2.1 and 4.2.2 depict phase (δ) measurements from dynamic frequency sweeps performed with MCR 702 and PZR1. All tests were performed in the linear regime. Data are shown for PDMS samples 1000,100 and 12.5 (number indicates η value in Pa s). Important observations here are:

- a. There is always a frequency-independent phase offset between PZR1 and MCR 702. Its value is 6.3° for PDMS 1000 and reaches 9° for PDMS 12.5, suggesting an increase for softer (thinner) samples. PDMS 100 data suggest an offset slightly above 6.3° .
- b. For weaker fluids, MCR 702 internal correction algorithm loses grip at around 45 Hertz. This is more evident in fig 4.2.2 with a profound discontinuity in the δ plot for the weaker 12.5 Pa s sample. Thus, measurements above 30 Hz are considered as “indicative”.

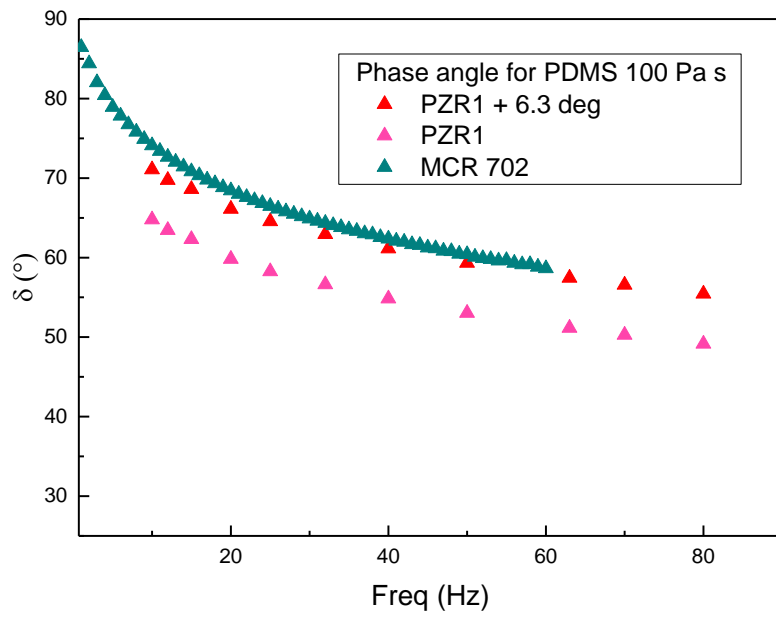
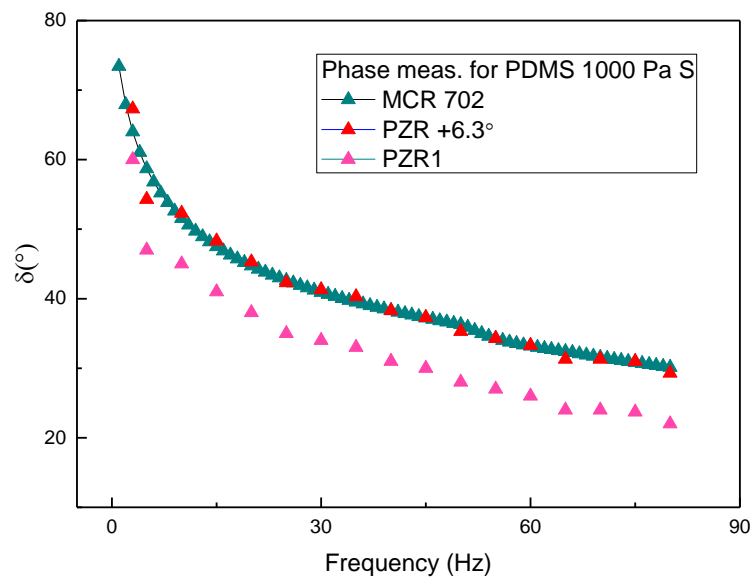


Figure 4.2.1 Phase angle measurements for PDMS oils with η 1000 Pa s (top) and 100 Pa s (Bottom). PZR1 data are shifted by 6.3° to match MCR 702 ones.

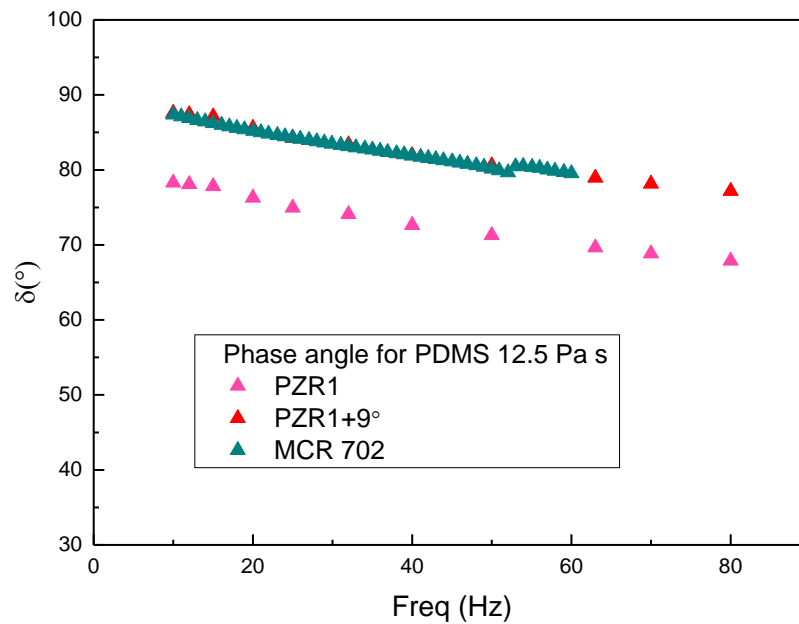


Figure 4.2.2 Phase angle measurements for PDMS oils with η 12.5 Pa s. Data has to be shifted by 9° to match MCR 702

The same behavior (phase offset) was observed when repeating the tests with other standard fluids, suggesting that the offset is viscosity-dependent as will be discussed further below.

The magnitude $|G^*|$ measuring loop must also be calibrated considering that our device measures the corresponding value in terms of voltage. Millivolts could be converted to stress and finally modulus magnitude, if multiplied by a correction factor (N) that reflects sensor sensitivity, amplifier gain, sample area (cross section) and gap dimension (consider that strain is gap and amplitude dependent). This factor should be material-independent thus calculated once for each gap setting. However, determining the gap is not a very accurate procedure in our setup. We chose to calculate the magnitude of the normalization factor N more often by matching magnitude values of PZR and MCR at overlapping range. This increases accuracy, trading-off with the PZR dependence on another (albeit standard) instrument. Fig 4.2.3 below depicts magnitude matching with a normalization factor $N=475$. Matching is done at 20Hz as MCR data above 30 Hz are considered, “indicative”.

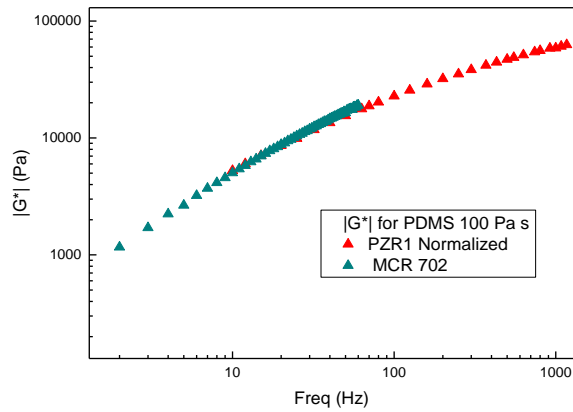


Figure 4.2.3 Magnitude data for the 100 Pa s PDMS oil standard. PZR1 voltage measurements were normalized by $N = 475$ to match MCR 702 at 20 Hz.

As a result of the above procedure, the viscoelastic data are reported in terms of phase angle (δ) and magnitude ($|G^*|$) for each measured frequency. Dynamic moduli (G' , G'') can be then calculated and their plots constructed by using their definition equations:

$$G' = |G^*| \cdot \cos(\delta) \text{ and } G'' = |G^*| \cdot \sin(\delta) \quad (4.1)$$

Figure 4.2.4 below shows the first DFS of PZR1 plot of PDMS1000 along with respective data taken with similar device by Roth and colleagues (Roth, D'Acunzi et al. 2010). Our data are slightly scattered due to crosstalk and noise that will be corrected.

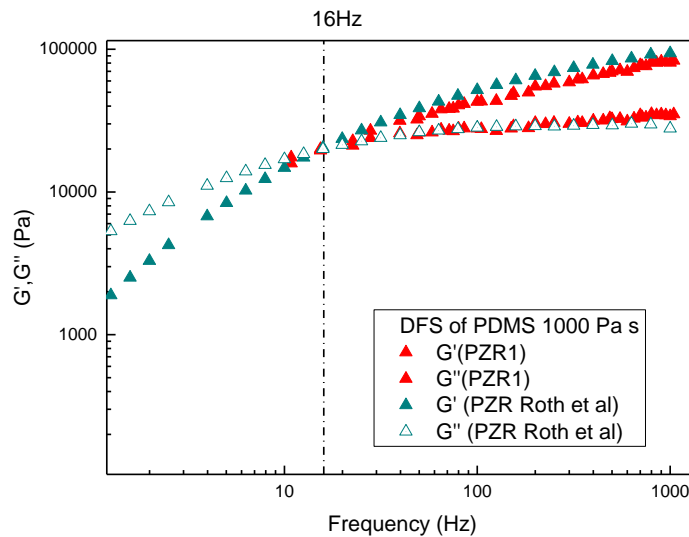


Figure 4.2.4 DFS performed with two different PZR1s. Our PZR1 and similar setup in Max Planck Institute for Polymers. Both devices present the moduli crossover at around 16 Hz while the specified value is 19.5 at 25°C also verified by MCR 302 measurement.

4.3 Calibration III and Validation: Linear Poly Butadiene (PBd)

Calibration II built confidence and gave an error indication for measurements up to 50Hz for time and stress sensing loops, but more experimental data were needed to validate measurements at least up to 1kHz. Also, the upper frequency limit of the instrument had to be experimentally defined. As discussed in chapter 3, dynamic data can be time- and temperature-shifted for thermo-rheologically simple materials, in our case linear Polybutadiene. Five samples were prepared in total as shown below:

Sample ID	Entanglements per chain (Z)	Polymer	Solvent	Comments
L70	70	PBd 133K Melt	No	Too stiff (PZR2)
L12	12	PBd 24K Melt	No	Ideal (PZR1)
L9	9	PBd 24K 75%	Squalene	Ideal (PZR2)
L6	6	PBd 24K 50%	Squalene	Within range (PZR1,2)
L3	3	PBd 47K 13%	Squalene	Too thin (PZR1) Within range (PZR2)

The two melts and the three solutions had different entanglements per chain Z, allowing to tune stiffness and relaxation times as described in Chapter 2. For solutions (L9, L6 and L3), cyclohexane was used as a co-solvent, with squalene. Removal of volatile co-solvent was possible under vacuum at room temperature. Antioxidant 2,6 Di-tert-Butyl-P-cress was added before dilution. Loading samples L70 and L12 was challenging due to stiffness. Holding screws can apply enormous pressure on the sample plates. In this case, the sample was squeezed (before loading) down to 200 μ m films, between two external glass plates (spare glass quartz plates) held apart with spacers. Relaxation was augmented by raising the temperature to 40 $^{\circ}$ C. Then the film was placed on the bottom sample holder of PZR1 and gradually squeezed as the cell was put together. The whole cell was placed again in the oven at 40 $^{\circ}$ C for several hours and holding screws gradually tightened to avoid breaking of the glass plates. Sample L proved too stiff, with a very weak viscous component (G'') in our frequency range. This resulted in marginal phase variance from 2.5 $^{\circ}$ to 3.7 $^{\circ}$. Data of phase angle measurements were in reasonable agreement with TTS data, when shifted by 2 $^{\circ}$ as shown below in fig 4.3.1.

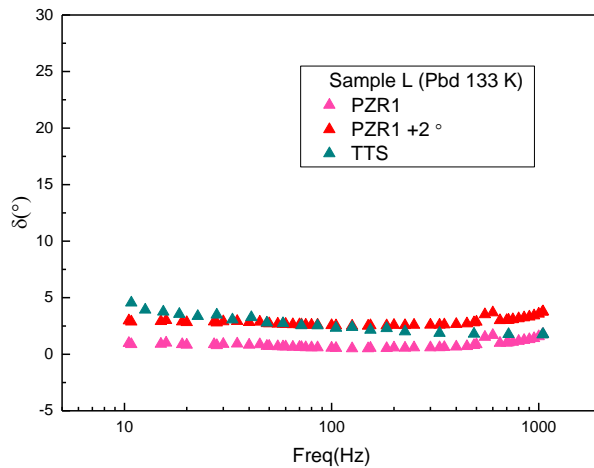


Figure 4.3.1 Phase angle measurements indicating weak viscous components for L70 (PBd 133K melt) taken with PZR1 against TTS data at $T_{ref}=25^{\circ}$ C.

In addition, the cell's lateral support was proved not adequate for very stiff samples such as sample L. Following the above we prepared sample L12, tuned to be our "favored candidate". The first crossover of dynamic moduli, corresponding to reptation time τ_d , falls well into the parametric envelope of PZR1 as shown below in figure 4.3.2. Dynamic Frequency Sweeps were performed at various temperatures (10,0,-20,-40 and -60° C) with ARIS rotational rheometer (TA Instruments, USA) at 3% stain. Dynamic moduli were time-temperature shifted to $T_{ref} = 25^{\circ}$ C, in order to and thus construct the L12 master-curve. L12 was also measured with PZR1 (DFS). The dynamic moduli superimpose well, as shown in Fig 4.3.3, by applying phase shifting of 2° like in sample L70.

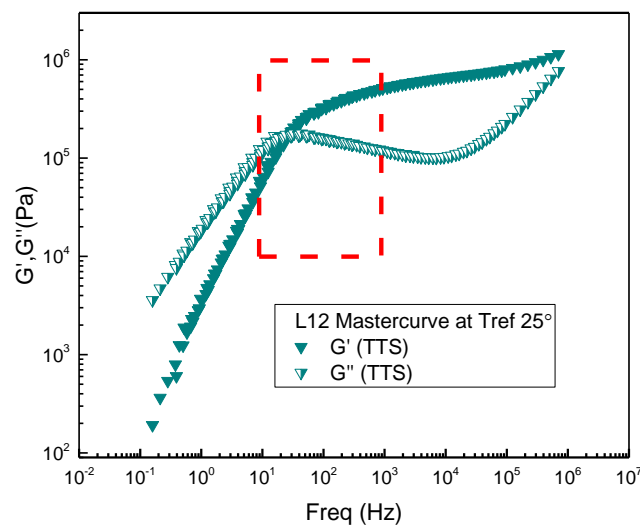


Figure 4.3.2 TTS Mastercurve for L12(Linear PBd melt 24K) at $T_{ref}=25^{\circ}$ C (data taken under D. Parisi guidance)

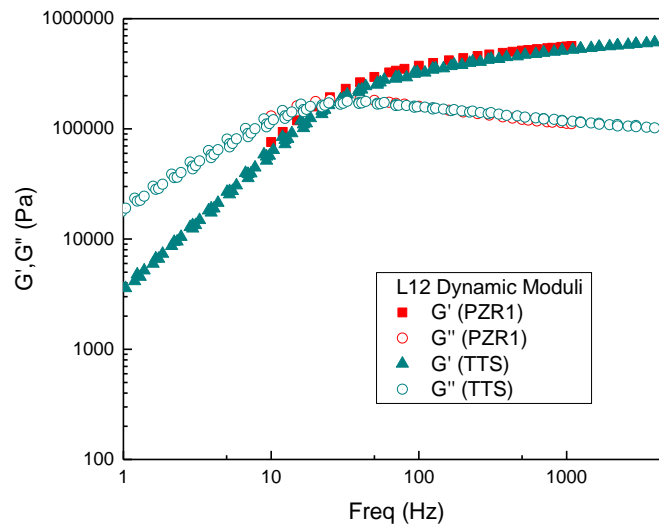


Figure 4.3.3 DFS data taken with PZR1 for L12 plotted against TTS data, present good agreement

To further validate our data we performed similar tests with samples L9, L6 and L3. We compare raw data, i.e. modulus $|G^*|$ and phase angle (δ). PZR1 data of phase for L12, L9 and L6 samples agree well with TTS data when shifted 2° for the first and 5° for the other two samples as shown in fig 4.3.4 and 4.3.5. However, phase angle data for the weaker L3 seem inconsistent even at higher frequencies where signal increases in strength. On the other hand, the magnitude data seem to agree, providing the second clue that phase angle measurements are more sensitive (fig 4.3.6).

Regarding **phase shifting** we can conclude that:

- Within test parameters it is frequency and phase angle (time)-independent and magnitude dependent.
- Qualitatively, this offset could be due to Piezo hysteresis as discussed in section 2.3
- Phase angle independence strengthens the view that offset is not related to any other factor, e.g., the glue used to secure the piezo elements
- A shifting of 5° is required for samples with viscosity similar to L9 and L6, while for stiffer samples (L70 and L12) a 2° shifting applies. For intermediate range more calibrating samples should be used or an interpolated value could be used with an error $\pm 1.5^\circ$ in phase angle.

Up to now we have also observed:

- Phase measurement difficulty in weak viscoelastic responses. Magnitude measurements seem more consistent even when the signal is weak and noisy.
- A small increase in phase angle at high frequencies conforms to the idea that it could be due to wall slip (Yoshimura and Prud'homme 1988) as discussed in section 3.3.3. Sample inertia would have caused the opposite effect, decreasing phase angle (Läuger and Stettin 2016).

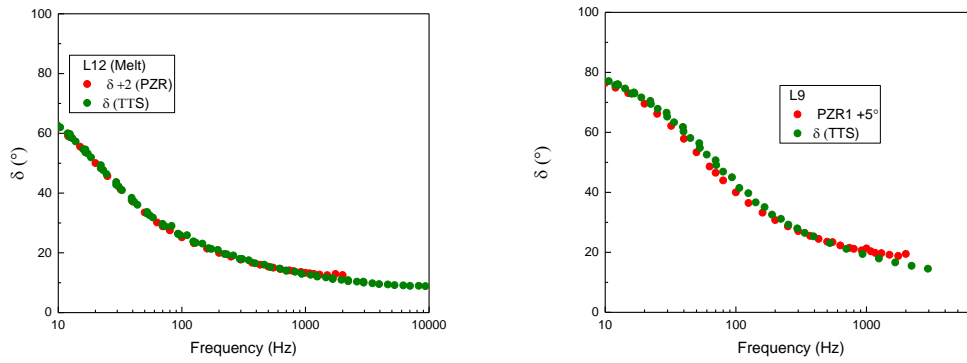


Figure 4.3.4 Phase angle data taken with PZR1 for L12 (left) and L9(right) against TTS data present good agreement when properly shifted. There is a slight increase of phase angle at high end more profound in weaker structured samples

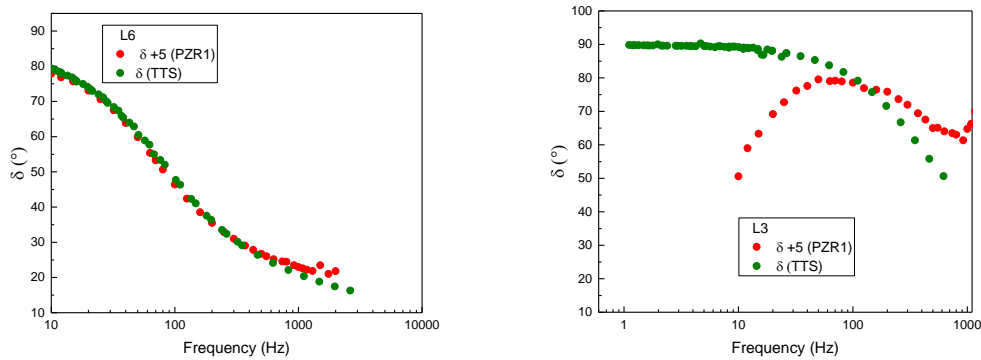


Figure 4.3.5 Phase angle data taken with PZR1 for L6 (left) and L3(right) against TT .L3 data are inconsistent. In both plots there is an increase of phase angle at high end more profound than L9.

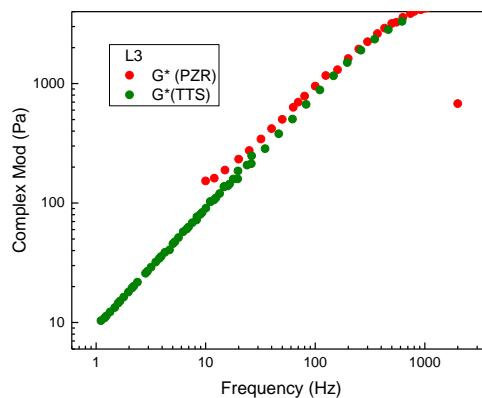


Figure 4.3.6 Magnitude data taken with PZR1 for L3 against TTS present better agreement despite phase measurement inconsistency

In order to increase sensitivity, PZR2 was constructed, capable of double displacement as described in section 2.3, double transducer sensitivity and with 2.6 times larger sample cross section. Theoretically, its sensitivity is enhanced by one order of magnitude and, as expected, can measure the

weaker L3 sample as shown in fig 4.3.7, and also perform better with weaker colloidal systems, as will be discussed in the next chapter.

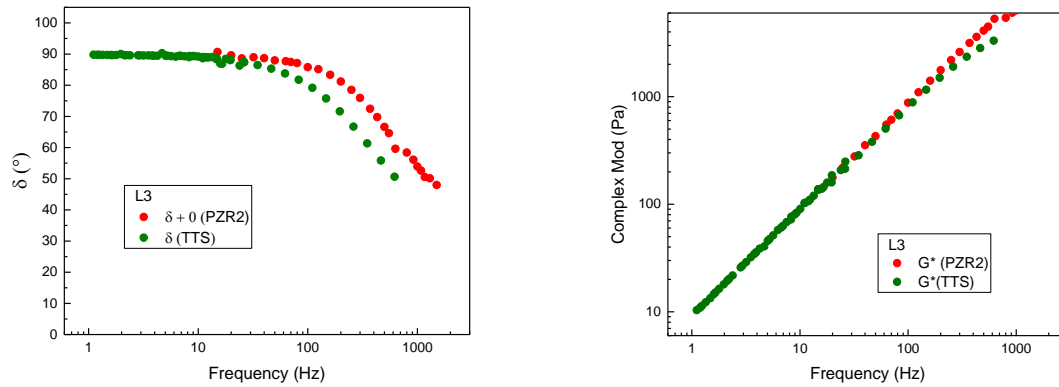


Figure 4.3.7 Phase angle and magnitude data taken with PZR2 for L3 against TTS present sufficient agreement than PZR1. Note no phase shifting was necessary.

Phase angle measurements are overestimated even at 100 Hz, displaying the same trend with stiffer samples but now in a more profound way and at lower frequency. This overestimation seems to increase with frequency and possibly fluidity and decrease with sample viscosity. It sets the lower sensitivity limit of PZR2.

Chapter 5 Colloidal HS Glasses: Results and Discussion.

We now turn our attention to HS colloidal glasses. We focus on high volume fractions of sterically stabilized PMMA spheres with hydrodynamic radii varying from 106 to 640 nm. Samples were prepared as shown below:

Sample ID	R (nm)	ϕ	Solvent	Frequency and $ G^* $ at 2 nd crossover (Hz/Pa)	Remarks
ASM 289 I	196	0.624	Octa-decene		Severe aging observed
ASM454 II	330	0.609	Squalene	9.55/39 (PZR1)	
ASM330 IV	132	0.61	Squalene	169/464 (PZR1)	
				153/530 (PZR2)	
ASM 50 VI	405	0.65	Squalene	125/479 (PZR1)	Creep test performed
ASM330 VIII	132	0.614	Squalene		To be measured
ASM 338 IX	625	0.59	Squalene	Low frequency	Second crossover is at low freq. Too low even for MCR702
ASM 340 VI	137	0.613	Squalene	160/589 (PZR1)	Measured also with multi speckle DLS
				260/963 (PZR1)	Aged 7 days
ASM 446 S1	106	0.6	Squalene		
ASM446 S2	106	0.58	Squalene	37.08/62.7 (MCR 702)	
ASM 446 S3	106	0.56	Squalene	18/31 (MCR 702)	

All volume fractions were determined by calculating the response at $Pe_0=0.5$, based on data obtained with the MCR702 and comparison with literature (Koumakis, Schofield et al. 2008). Determining volume fractions from RCP proved ambiguous as sample quantities were small and often the minute amount of remaining solvent after removing the supernatant, following centrifugation, changed dramatically the calculated fraction. Note that the solvent added in some cases was just a drop (ASM 50VI).

5.1 Linear Rheology of Hard Sphere Glasses and Aging

Figure 5.1.1 compares DFS data taken with Anton Paar MCR 302 and PZR1. The former was apparently operated above its frequency limit, as its internal correction loop lost “grip” at approximately 30Hz. The trend of LVE curves obtained with PZR1 appears reasonable and physical. The HF crossover was reached and the magnitude was again matched at 20 Hz in order to minimize gap determination error.

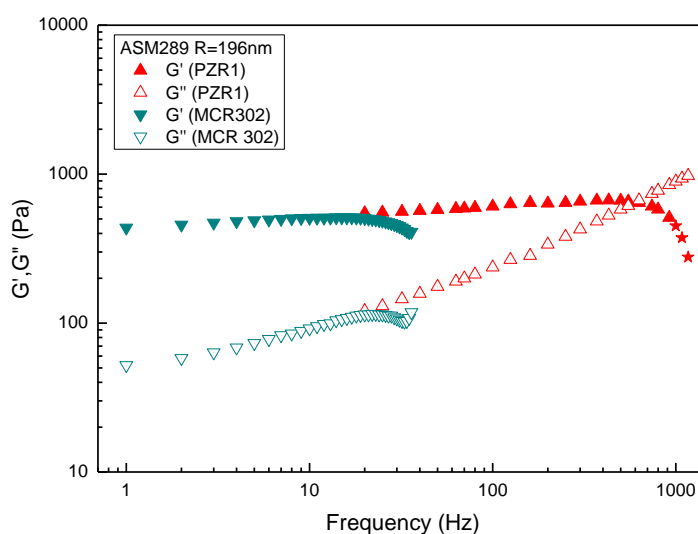


Figure 5.1.1 DFS data for PMMA particles suspended in Octadecene taken with MCR 301 (CMT configuration) and PZR1

The downturn in storage modulus after the HF crossover indicated by star symbols, is considered to be an artifact and will be discussed below. Refractive index mismatch between solvent and PMMA induces attractions and “contaminates” the theoretically pure repulsive potential, under the condition that the stabilizing layer does not balance out this effect. This explains, in part, the time evolution of the moduli (fig. 5.1.2 left), a phenomenon known as aging (Ballesta and Petekidis 2016),(Negi and Osuji 2010) (Koumakis, Schofield et al. 2008). Comparison of Dynamic data for similar particles dispersed in Octadecene and Squalene (fig 5.1.2) show a minimal aging behavior of dispersions in the latter solvent where refractive index is better matched. Since conventional large-amplitude rejuvenation is not possible with the PZR, all measurements were performed within 30 min of loading and combined with data obtained with CRR using a similar protocol, in order to confirm the absence of strong aging. It is fair to say that a proper aging study should compare the same particles in terms of size and polydispersity. There is no “non-aging” glass but we have found that in some cases the linear viscoelastic moduli are not affected significantly during measurement time. What is more important in our case is that aging seems to affect more lower frequencies, as observed in fig 5.1.3 (left), conforming to literature findings (Ballesta and Petekidis 2016). On the other hand, sample

ASM 340 VII exhibited gradual stiffening after 7 days, as seen in fig 5.1.3 (right). Solvent evaporation is likely not reason for this, considering the low vapor pressure of Squalene. A small amount of Squalene was also tested for evaporation at room temperature over 21 days with no indication of mass change. Nevertheless, we tried to conduct all measurements within 30 min upon loading, followed by equilibration (rest time) of about 10 min.

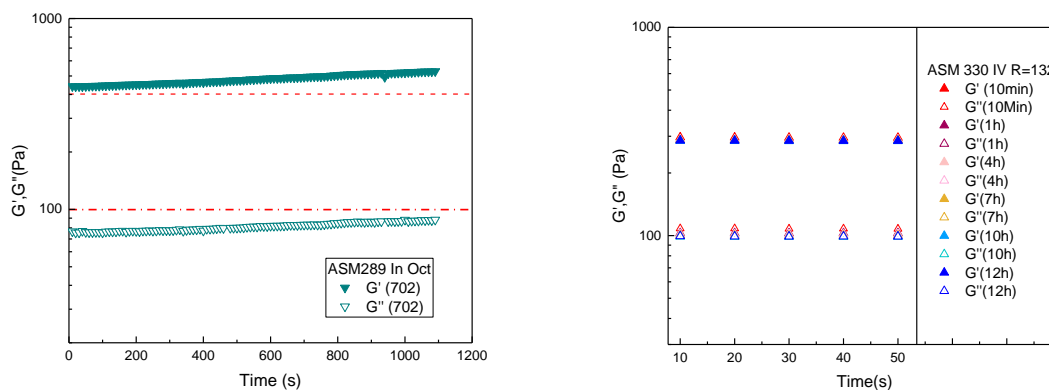


Figure 5.1.2 Dynamic moduli at fixed frequency 10Hz plotted over time portraying dissimilar behavior between severely aging sample within 1000 sec (left) and almost nondetectable aging (right) within 12 hours period.

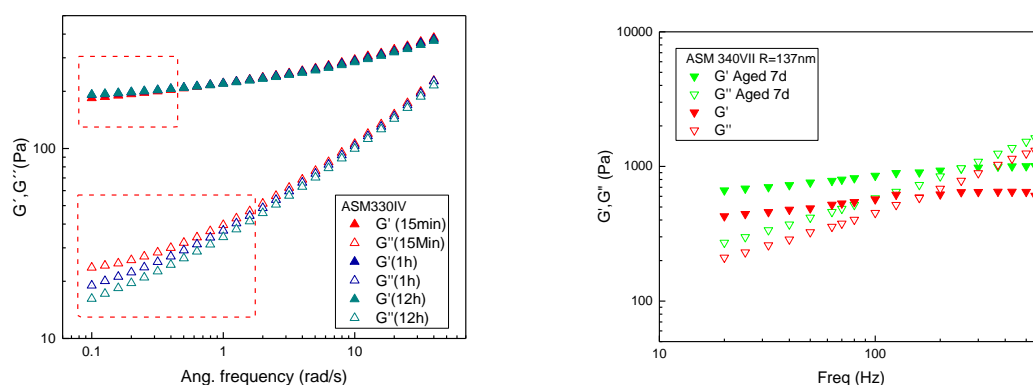


Figure 5.1.3 Dynamic moduli time evolution at low frequencies for ASM330 (left) and ASM 340 (right)

Figure 5.1.4 below depicts similar data for the R=132 nm HS glass. The high-frequency moduli crossover (left plot) occurs at $\omega_{2c} = 143$ Hz as smaller volume fraction leads to less constraint (looser) cage and slower in-cage rattling. At shorter times the G'' data follow a straight line with its slope indicating η'_{∞} . The storage modulus tends toward a plateau but then experiences a significant, albeit unphysical drop marked in yellow. This behavior is due to an overestimation of the phase angle, whose values exceed 90° as can be seen in Fig 5.1.4 (right). The loss modulus is less affected as sine function is less sensitive around $\pi/2$.

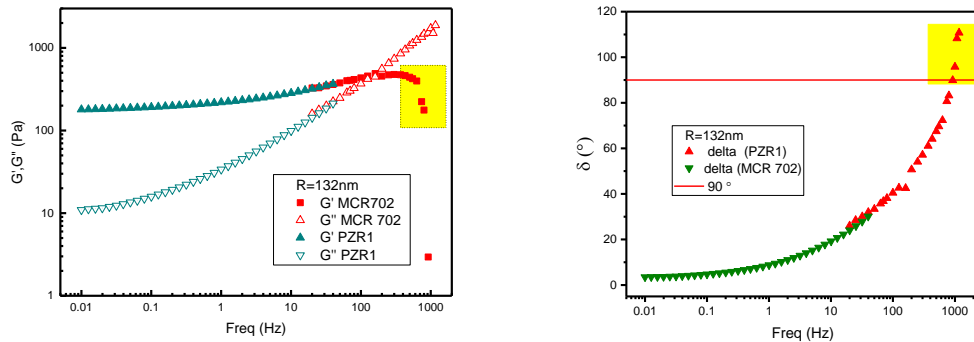


Figure 5.1.4: DFS test data for ASM330 IV taken with MCR702 (cyan symbols) and PZR1 (red symbols) at 25° C.

This error confirms that phase measurements are trickier. Had the cause been noise or other interference, the error would have decreased with signal strength. However, even with stiffer samples displaying larger magnitude (stronger signal), this behavior was repeated whenever the phase indicated proximity to Newtonian behavior. We emphasize that this is the only detectable difference when the instrument measures linear PBd samples and colloidal glasses around 500 Hz. It has been shown (Velankar and Giles 2007) that measurements are indeed more difficult in the Newtonian limit (9°). From a completely different perspective, as discussed in section 2.2, it has been shown that the deviation (error) in phase angle is larger in the Newtonian limit rather than the solid regime, with estimated errors for $\lambda/5$ sized gaps of 29.6° and 3.3° , respectively (Schrag 1977). This leads to huge errors in moduli when considering the sensitivity of $\tan(\delta)$ at the limits of 0 and 90° .

To support our conjecture and also improve the accuracy of our data, an analysis based on the Kramers-Kronig (KK) relations, based on causality principle, was performed. We used the suggested interconnection between magnitude and phase (Booij and Thoone 1982), as analyzed in section 2.1.5. A consistency check was performed first with the rheologically simpler linear PBd 24k. We fed moduli data from the master curve shown in fig 4.3.2 to equation (2.8) and calculated the phase angle. This simulates the case of measuring only the magnitude and extracting theoretically the phase angle. Figure 5.1.5 (left) shows the so-extracted phase angle (KK) plotted against the measured one (TTS), demonstrating reasonable agreement. A colloidal glass is more complicated, but since causality and linearity are linked, the approximation should hold. Figure 5.1.5 (right) compares dynamic moduli for $R=405$ nm hard spheres derived from measurements and the prediction based on Kramers-Kronig relation based on equation (2.8). Remarkably, the significant drop of experimental G' has been eliminated, while G'' exhibits the same frequency dependence, yielding the same η'_∞ . At frequencies below the crossover, the measured and predicted moduli are in very good agreement, as expected.

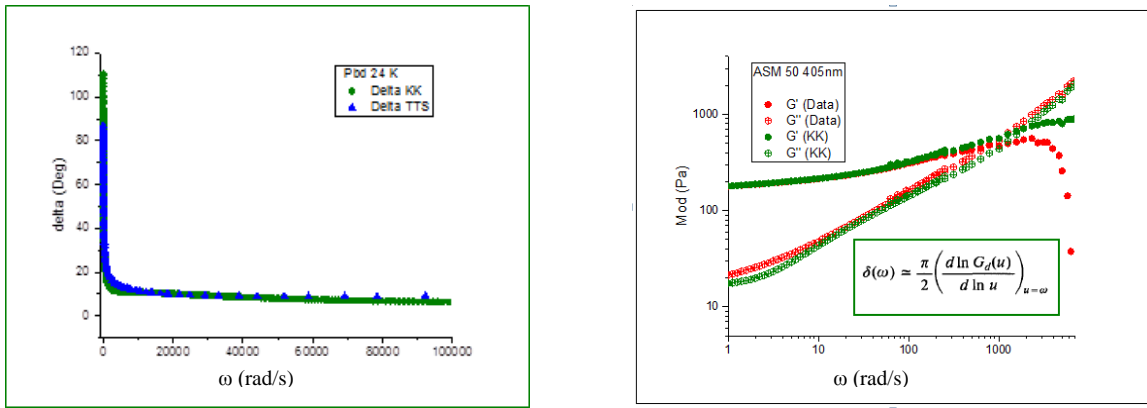


Figure 5.1.5 Left : TTS derived phase angle plotted against KK derived phase angle for linear PBd sample L12. Right: DFS plot for a very dense glass taken with PZR1 against the KK derived one. Notice that the DFS and KK loss moduli (G'') are in good agreement even at high frequencies

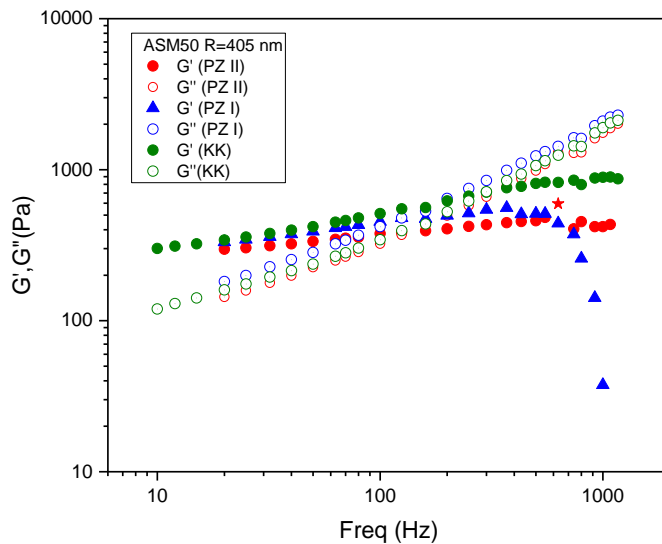


Figure 5.1.6 DFS data taken with PZR1 and PZR2. Green symbols show PZR1 data corrected by KK approximation (equation 2.8). Red star denotes PZR2 resonance at 680 Hz. Deviations are expected as the sample is very dense

5.2 Scaling laws above high-frequency crossover

At first glance and for ideal hard spheres, the elastic component is due to Brownian forces acting as springs against the relatively quickly imposed deformation and the viscous one due to dissipative interactions (Mewis and Wagner 2012). Theoretically, the moduli can be normalized by the thermal energy per particle volume and the frequency by the Brownian time, allowing for data comparison

between spheres of different size. However, there are significant deviations from this scaling at high frequencies and volume fractions (Russel, Wagner et al. 2013),(Mewis and Haene 1993) as explained in Chapter 3. Dynamic localization theories (DLT) have been developed to characterize suspension mechanics for strongly interacting particles and capture the scaling of G' with volume fraction and its frequency dependence. Consequently, our approach will focus on comparing experimental observables with scaling predictions at high frequencies available in the literature, focusing in particular at the limiting behavior of G' , G'' and the crossover time.

5.2.1 Elastic Modulus

Figure 5.2.1 depicts the limiting behavior of large spheres at high-frequencies that lies within CRR frequency range. G' data extracted from measurements with both ARES and MCR 702 rheometers exhibit a weak power law (slope 0.425), consistent with results with torsional resonators (Fritz, Pechhold et al. 2003), but in contradiction with data with bare silica spheres (Shikata and Pearson 1994). Similar results are obtained with PZR2 up to 50 Hz where measurements become untrustworthy. Data scattering is due to weak signal. A 50 mm plate-plate geometry was needed in order to adequately perform the measurement with the ARES rheometer. The increase of the slope of G' versus frequency at the high-frequency end, for both ARES and MCR, is considered to be an artifact possibly due to inertia. Similar weak power-law limiting behavior is reported in fig 5.2.2 (left) where the 2nd (high frequency) crossover is accessed with CCR (MCR 702).

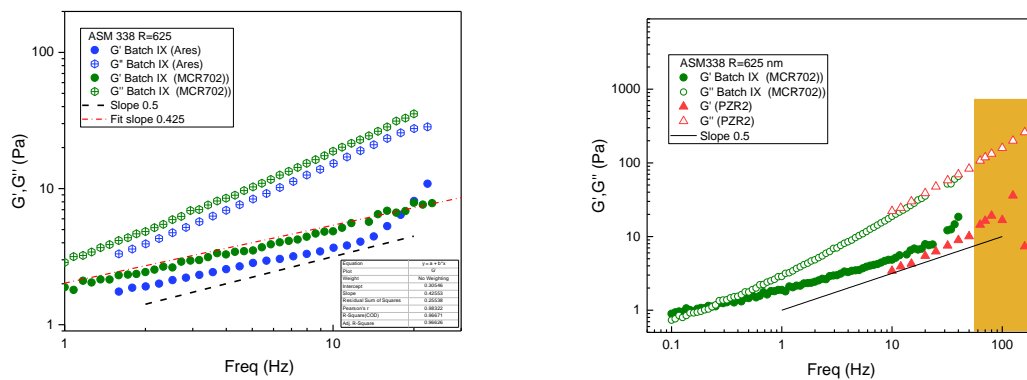


Figure 5.2.1 Dynamic moduli for large spheres $R=625$ nm. Left: Data taken with two different rheometers exhibit weak power law of G' (slope 0.425 red dashed line). Right: Data taken with PZR2 confirm weak power law. The elastic component is too weak to be detected (shaded area) at high frequencies.

In an attempt to confirm the cause of phase angle overestimation, we compare PZR1 with PZR2. As discussed above, PZR2 is more sensitive by construction, thus its response signal is stronger. Also the glass plates are made from different material, BK7, compared to PZR1's quartz. Fig 5.2.2 compares the conventional and PZR1-based DFS data of fig 5.1.5 against the data obtained with PZR2. The

latter do not exhibit the unphysical drop of G' at the highest frequencies, however some deviations from the data based on PZR1 are observed throughout the entire frequency range. This may be due to the fact the the sample may be too stiff for PZR2 or to heterogeneities and residual stresses from loading history expected in a very dense glass with $\phi=0.65$. Nevertheless, this plot is considered useful in determining the mechanism behind G' drop.

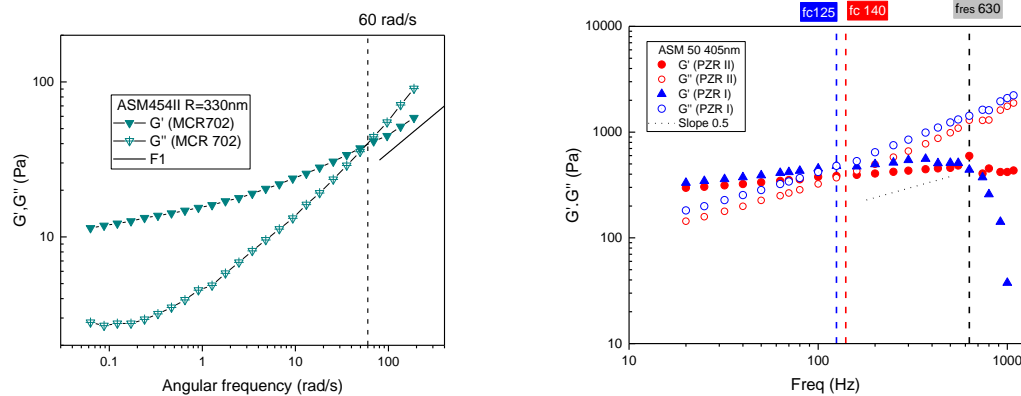


Figure 5.2.2 Left: DFS plot taken with MCR 702 captures elastic modulus limiting behavior. Right: DFS plots for a very dense glass of spheres $R=405$ nm taken with PZR1 and PZR2. Dashed blue, red and grey lines indicate 2nd crossover frequencies for PZR1, PZR2 and resonance for PZR2, respectively.

Wall slip can neither be excluded nor absolutely confirmed, but it is likely to affect measurements with phase overestimation, in qualitative agreement with literature (Yoshimura and Prud'homme 1988). The entire response spectrum can be considered including contributions from nonlinear phenomena and instabilities including wall slip. Consequently, the presence of even harmonics associated with wall slip in Large Amplitude Oscillatory Tests (Yang and Yu 2017) serves as an indication rather than proof (Cloitre and Bonnecaze 2017).

Surface texture and chemistry have also been found to affect slip. Contact angle measurements for Squalene drop on PZR1 quartz and PZR2 optical BK7 plates indeed yielded values below a few degrees (fig 5.2.3). The nearly total wettability of the used polished glass plates in Squalene could enhance wall slip through the formation of a continuous lubricating film where particles are depleted (Cloitre and Bonnecaze 2017).

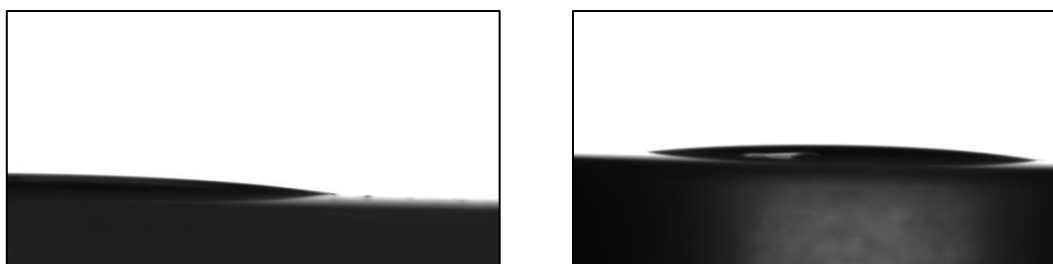


Figure 5.2.3 Images of solvent drop (Squalene) on PZR1 (left) and PZR2 (right) glass plates. Contact angle is below the instrument's detection limits.

5.2.2 Viscous modulus and Dynamic viscosity.

The dynamic viscosity limiting value (η'_{∞}) can be calculated from the slope of the viscous component versus frequency (G''/ω) in the double logarithmic plot. Figure 5.2.4 shows the calculated values of reduced dynamic limiting viscosity ($\eta'_{r,\infty}$), i.e., normalized by solvent viscosity (0.015 Pa s), as compared with two semi-empirical formulas. The dashed and the solid green lines depict the respective equations

$$\eta'_{r,\infty} = \frac{1+1.5\varphi(1+\varphi-0,189\varphi^2)}{1-\varphi(1+\varphi-0,189\varphi^2)} \quad for \ 0 \leq \varphi < 0,64 \quad (\text{Lionberger and Russel 2000}) \quad (5.1)$$

and

$$\eta'_{r,\infty} = 15.78 \ln\left(\frac{1}{1-1.16\varphi^{1/3}}\right) - 42,47 \quad for \ 0,60 \leq \varphi < 0,64 \quad (\text{Cheng, Zhu et al. 2002}) \quad (5.2)$$

Equation (5.1) is based on data observations in relatively monodispersed bare silica particles with hydrodynamic radii 53, 155 and 202 nm up to volume fractions of 0.54 (Shikata and Pearson 1994) hence exhibits good agreement with lower volume fraction samples. On the other hand equation (5.2) (Cheng et al., 2002) is based on simulations of particles undergoing Stokes flow (low Reynolds number) ignoring Brownian forces (Sierou and Brady 2001). It exhibits better agreement at high volume fractions as hydrodynamic contribution is included, nevertheless it underestimates the viscosity possibly due to the fact that Brownian and steric layer contributions are ignored and to the uncertainties in determining the volume fraction. Polydispersity will also shift RCP to higher fractions, hence the distance from maximum packing ($\varphi_{\max} - \varphi$) should be a more appropriate parameter for the viscosity evolution, rather than the absolute φ . The data point corresponding to ASM50VI (square) is way off predictions. A series of measurements has to be repeated as the origin of this behavior is unknown. Taking into consideration the increased φ of this sample density heterogeneities and presence of wall slip should be examined.

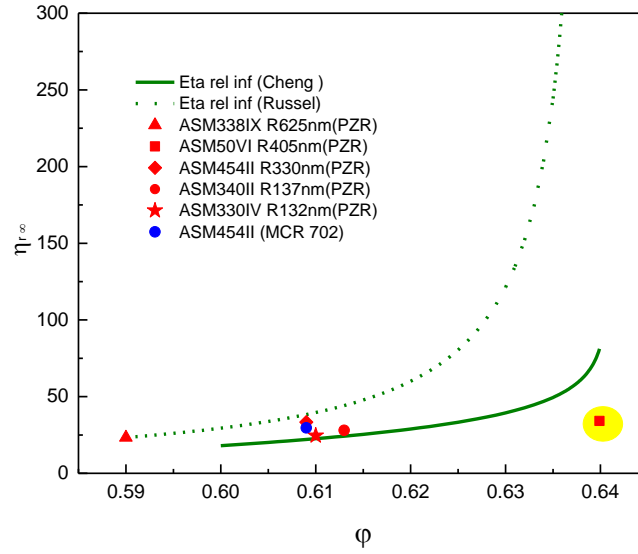


Figure 5.2.4 Dynamic frequency limiting behavior ($\eta'_{r,\infty}$) from PZR measurements (red symbols), MCR 702 (blue) and semi-empirical equations 5.1 (green dashed line) and equation 5.2 (green solid line).

5.2.3 Time scaling derived from “Trap” model

As discussed in section 3.3.1, dynamic localization and entropic trapping can describe dynamics of dense glasses. The localization length (r_{loc}), the displacement where restoring forces maximize (R^*) and the barrier displacement where mechanical work is maximized (R_{MW}), can be distinguished from their volume fraction dependence (Schweizer and Yatsenko 2007):

$$r_{loc} = e^{-12.2\phi} \cdot R \quad (5.3)$$

$$R^* = 3.3 \cdot e^{-6.6\phi} \cdot R \quad (5.4)$$

$$R_{MW} = 3.3 \cdot e^{-6.6\phi} \cdot R \quad (5.5)$$

. Equation (5.5) describes the barrier limit, defined by the maximum work (MW) required to be spent by an overcoming particle. As a result only a “few” particles will eventually overcome this barrier, within a certain time frame, after attaining enough kinetic energy, larger than MW mean value. This is termed thermally activated hopping. Full theoretical calculations seem to agree well with equations (5.3-5) only in high concentrations $\phi > 0.55$, as shown in Fig 5.2.5. Therefore, for our subsequent analysis these approximations are adequate.

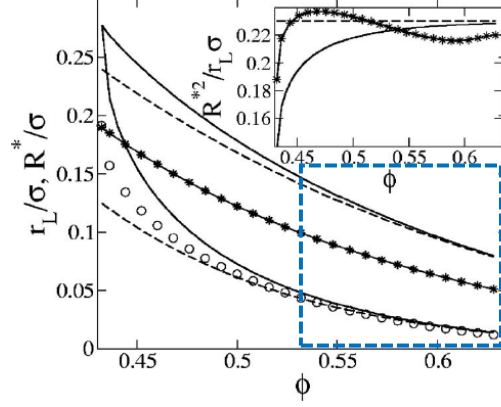


Figure 5.2.5 Localization length and maximum restoration force length normalized by particle diameter (here denoted σ) plotted against ϕ . Solid lines denote simple calculations from equations above and points full calculations. Blue square indicates range where full calculations agree with simplified equations From (Schweizer and Yatsenko 2007)

Considering a DFS plot we can assume that at times smaller than crossover time (τ_{CrH}) the particle feels no restrictions by its neighbors and displays almost Fickian diffusion (liquid-like behavior). However during the last part of this time, motion becomes sub-diffusive until caging is fully imposed, corresponding to the MSD plateau. Since τ_{CrH} marks this virtual solid-to-liquid transition, we assign it to an in-cage characteristic time. This is the maximum time taken for the particle to rattle within its cage covering a total rattling distance (r_{rat}), before interacting with its neighbors. By applying Fick's law:

$$D_s(\phi) \cong (r_{rat})^2 / 6 \cdot \tau_{CrH} \quad (5.6)$$

We can then calculate the rattling distance for an experimental derived time (τ_{CrH}) and the corresponding short time self-diffusion coefficient $D_s(\phi)$, taken from Stokesian dynamics simulations (Sierou and Brady 2001). Consequently the extracted rattling distance from the data should reflect the localization length ($r_{rat} \sim r_{loc}$) derived from DLT calculations as shown in fig 5.2.5. Figure 5.2.6 shows plots of the dimensionless rattling distance r_{rat} (normalized by particle radius) calculated from our experimental data against DLT predictions. The cyan solid line indicates the localization length while the black solid the barrier the related travel distance (with MW subscript denoting maximum work). The dashed line in-between indicates the distance where the traveling particle feels restoring forces to maximize (R^*). Our very dense sample (blue circle) r_{rat} is very close to the DLT predicted localization length. The rest of data overestimate the cage size with blue triangle and square being closer to DLT predictions. This indicates a trend towards larger deviation at lower concentrations. This trend is shown in fig. 5.2.7 left plot, whereas the right plot suggests almost a power-law behavior when the deviation is plotted against distance from maximum packing fraction (ϕ_{max}).

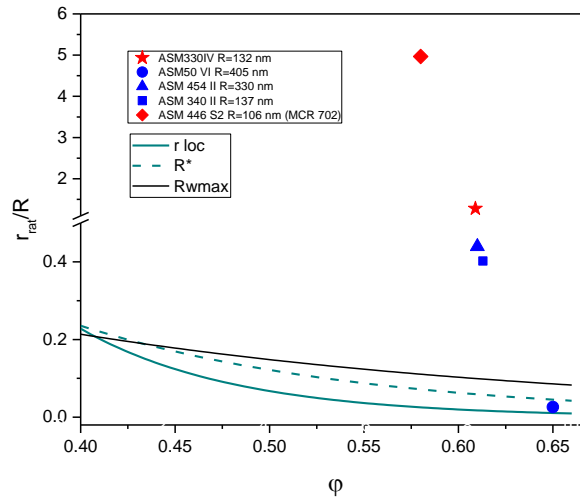


Figure 5.2.6 Dimensionless rattling distance (r_{rat}) calculated from experimental data (symbols) against theoretical calculations for localization length and distance that restoring forces maximize (R^*)

We believe that the main reason for this overestimation in r_{rat} is particle's sub-diffusive motion (slow down) during the last part of τ_{CrH} , before caging is fully imposed. Other sources of deviation could be uncertainties in sample volume fractions, DLT predictions and D_s calculations, the latter based solely on Stokesian Dynamics. These are formidable challenges and to address them a deeper investigation with more experimental data is necessary. Some initial comments can be made though in the next two paragraphs.

Considering the accuracy of our measurements, we should stretch that in dense glasses small uncertainties in volume fraction may lead to extremely large errors. This is also evident from the steep D_s slope in fig 3.1.2 (left plot) as the volume fraction approaches a value of 0.63. Density heterogeneities can also enhance the departure from expected HS behavior. The red symbols are way off the barrier limit and especially in the case of the smallest particle glasses with $R=106$ nm. This deviation could also be due to the steric layer softness although the trend in the plot of fig 5.2.7 suggests departure from predictions as concentration decreases.

On the other hand, DLT has *a priori* weak points. It includes strong phenomenological elements since a significant amount of physics is ad-hoc (Kobayashi and Schweizer 2005). This renders material-specific physics not possible to predict, for example the role of the presence of steric layer. We would expect large spheres to conform better to the predictions. This may be reflected in the deviation observed with small spheres but it needs to be further confirmed. A systematic approach should compare large, medium and small spheres plotting deviations against distance from ϕ_{max} and

R^3 . The distance of r_{rat} from the barrier and R^* displacement should also be considered and scaled.

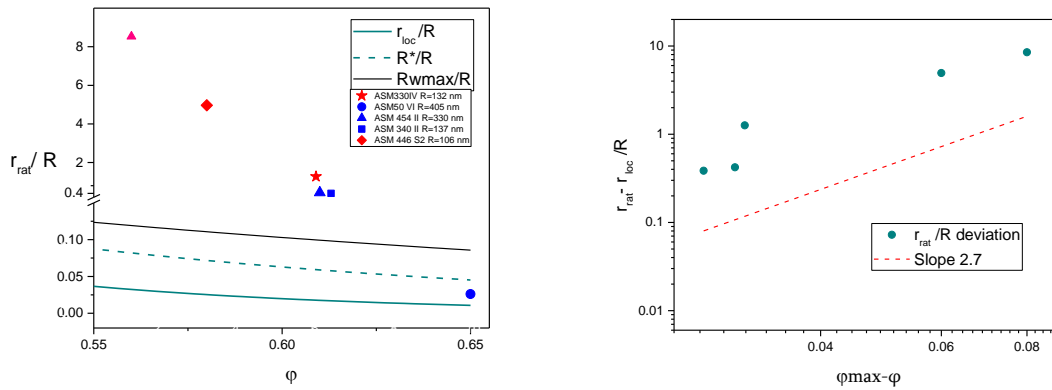


Figure 5.2.7 Left: Same data as Fig 5.2.6 in more detail show that deviation from theory is larger in lower volume fractions and small diameters Right : Deviation of reduced rattling length from theoretical localization length ($r_{\text{rat}}-r_{\text{loc}}/R$) as a function of $\phi_{\text{max}}-\phi$.

Nevertheless, this is considered as a first approach and as such it will generate more questions than answers building a robust pathway for future work. Bridging a microscopic theory (DLT) and bulk observations is definitely challenging.

5.3 Extending the Low frequency end of the spectrum

As mentioned above, our dense samples should exhibit fast β -related dynamics and large hopping times, thus we expect the terminal flow regime to fall well below the frequency capabilities of our PZR and MCR 702. In principle, a broader spectrum can provide better accuracy in δ and $|G^*|$ interrelations. This concept provided the motivation to extent the low-end by creep tests (Evans, Tassieri et al. 2009) and use the data with KK-based (Tschoegl 2012) to calculate phase angle from magnitude as above .

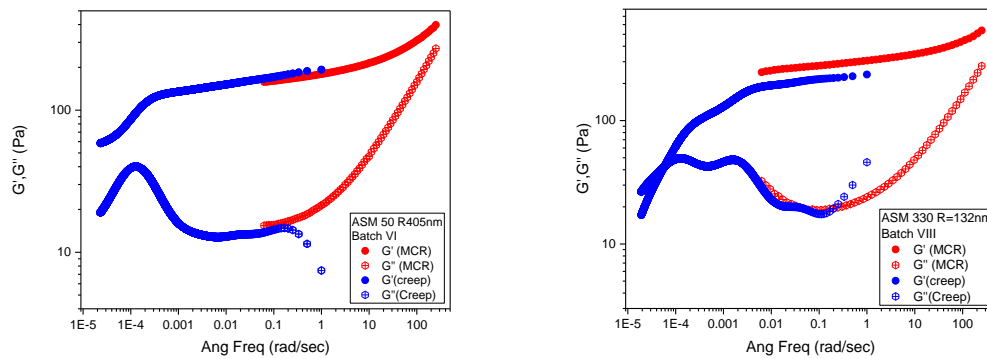


Figure 5.3.1 Dynamic moduli data taken with MCR 702 (red) extended to low-frequency range by creep test for $\phi=0.65$ and $\phi=0.614$. Script based on Evans et al, 2009 and script provided by Daniele Parisi

Figure 5.3.1 shows (blue symbols) creep derived data for two glasses. To increase the torque during measurements we used very dense large spheres (ASM50VI) and less dense smaller ones (ASM330VIII). In the denser sample (left) moduli agreement is quite satisfactory in the overlapping region with the DFS data. The onset of “alpha” relaxation is accessed but not fully captured. On the other hand, in the less dense ASM 330 we can see the terminal flow although there is significant data scattering possibly masked by the smoothing process in the algorithm.

Chapter 6: Conclusions and Recommendations for Future work

A sliding plate piezo rheometer has been developed and shown to provide a valuable tool for extending the upper frequency range of Commercial Rotational Rheometers. The technique has been validated by comparison with Time-Temperature superimposed data and fundamental mechanisms and error sources have been discussed. Colloidal hard sphere glass dynamics have been successfully probed in short times and data were compared against theoretical predictions.

6.1 Conclusions from the Piezo-Rheometry study

Piezoelectric Sliding Plate Rheometer seems to work quite well over the applied frequency range of 10 to 1000 Hz, the so-called *intermediate frequency region* and for moduli ranging from 10 to 10^6 Pa. Its simple construction guarantees less resonances and harmonics, whereas reduced cell lateral rigidity sets the upper limit in sample stiffness. The technique has been validated by comparison with TTS data in order to minimize errors related to intrinsic nonlinearities and noise interference. When used in conjunction with a CRR, gap uncertainties are removed and a broad spectrum DFS can be obtained with the combination of the two instruments.

Phase angle measurements present an increased difficulty especially in thin samples in the fluid-like time regime. Slip can be the reason that phase angle is overestimated above the second crossover. Furthermore, self-checking and correcting is feasible using linear response theory (Kramers-Kronig relation). This simple approach could be applied to any rheometric measurement in the linear regime.

6.2 Conclusions from the concentrated Hard Spheres study.

By implementing this technique the high-frequency dynamic moduli crossover has been detected in HS glasses. It is usually inaccessible with conventional rheometers with the exception of glasses with slow β -relaxation related dynamics (large spheres). The corresponding crossover times

and G'' limiting behavior have been compared with scaling laws in literature. Volume fraction determination is challenging for small volumes of samples near jamming, resulting in large errors. Data for the limiting dynamic viscosity comply with the scaling laws in the literature except for near-jamming fractions. The latter regime appears to be described well by scaling laws derived from trapping models. More data will be needed to reach a consensus. Increased frequencies in oscillatory tests provide the **magnification lens** on particle roughness, consequently our PMMA particles with their PHSA hair divert from hard sphere behavior as inform our measurements, in agreement with literature.

6.3 Future Work

Piezo rheometer has substantial room for improvement. Gap can be better determined by the use of micro-positioners. Actuator nonlinearities (hysteresis) can be measured with an optical method such as Michelson interferometer or commercial vibrometer. The displacement data, taken in sufficient small time steps, will describe actuator frequency response via a bode plot, providing answer to the origin of the observed phase angle offset. Furthermore wall slip effects should be explored, especially their possible effect in phase angle overestimation at increased frequencies and near jamming concentrations. Possible approaches include changing plate texture and material, i.e., using metallic unpolished plates instead of glass ones. The study of signal patterns with possible presence of substantial even harmonics may suggest but not prove wall slip. Beyond the oscillatory regime one can perform transient tests, i.e., step shear rate and step strain and recovery measurements, as discussed in Appendix B, or in general excite sample with an arbitrary waveform within instrument time response limits.

Our data can be further compared with similar ones obtained from indirect microrheological methods based on DWS or Multispeckle DLS. Furthermore, a considerable systematic study could challenge localization theory predictions with systematic measurements of small, medium and large spheres at different volume fractions combining Piezo-rheometry and optical methods. Finally, this technique could be applied to various complex fluids with rich relaxation spectra within 10 to 1000 Hz. Promising candidates might be HS attractive glasses, multiarm star glass formers, gels and emulsions. The list is endless.

Appendix A: Photographs and Plans

PZR 1 is shown in figure A1. Plate alignment is achieved optically by shedding laser light perpendicular to the glass plates. Reflection from each plate side (air-solid interface) will result in distinct speckles that can be captured by means of a camera or projected on a screen i.e white wall. By selectively treating the glass surfaces with antireflection coating for the used wavelength (632nm) one can eliminate unwanted speckles to make alignment easier. PZR2, shown in fig. A2 has stainless steel-aluminum holder plates therefore a hole on the top plate (not shown) provides optical access to the sample plates. Plate alignment can be also verified by spacers.

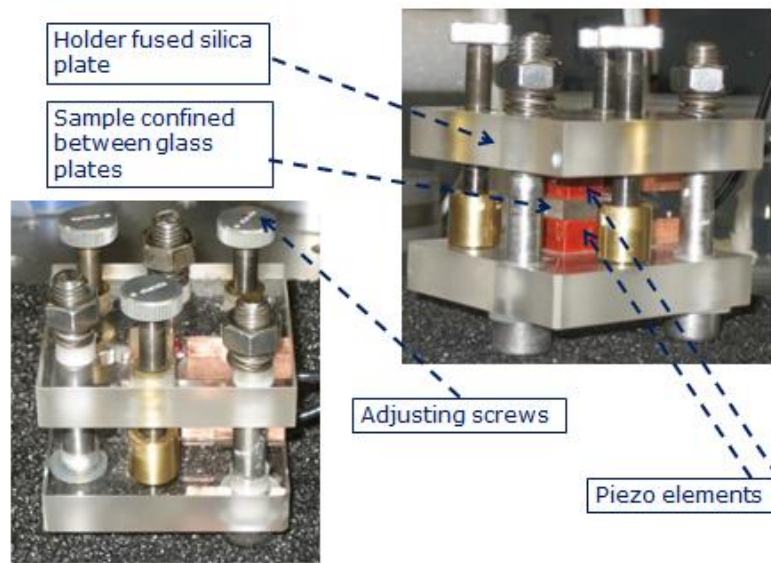


Figure A1 PZR1 fully assembled

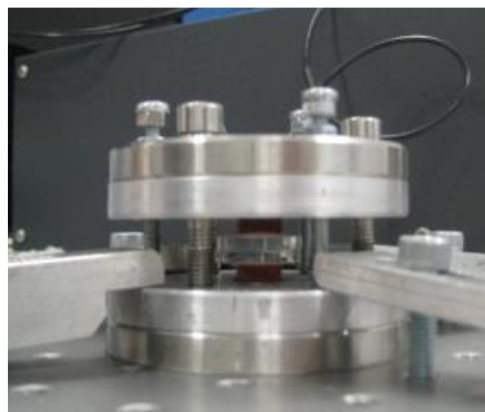


Figure A4 PZR2 Assembled, loaded and firmly secured on the table

PZR schematic is depicted in fig. A3. Each holder plate consists of two disks one made of stainless steel and the other of aluminum to ease fabrication. The central rectangular hole and the groove in the aluminum plates form a recess (housing) to provide the vital EMI shielding to the piezo transducer and its cable.

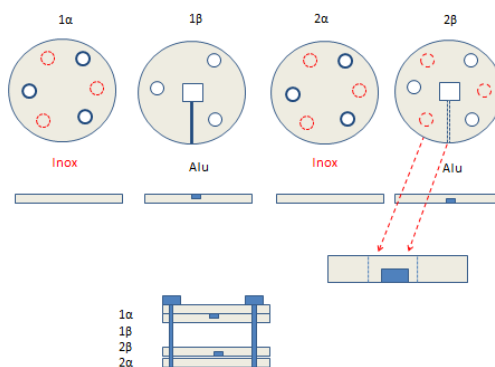


Figure A3 PZR2 details

Appendix B: Transient Tests

Considering the various periodic waveforms that can be generated by the function generator, it is easily seen that one can impose various deformation patterns. As a result transient strain control experiments can be performed as long as the measurement can be completed within times smaller than the period of the signal. These times on the other hand, cannot be too long (>1 sec) as *ferroelectric* creep can affect measurement as discussed in chapter 2. Rheological creep tests cannot be easily performed for the same reason and the inability to control the applied stress with this setup. We demonstrate two examples of these tests in order to induce motivation for future work. Although the response waveform can be easily obtained in the oscilloscope, the analysis should be made with caution as the signal can be distorted by the charge amplifier filters i.e. each Fourier component (sine wave) is phase shifted according to its frequency.

In order to perform the so called **step strain test**, the excitation can be a square waveform with sufficient period to capture the full relaxation spectrum. The stress response to the step strain divided by the imposed strain derives the relaxation modulus. Figure B.1 left shows sample L12 (PBd 24k) stress generated signal (red curve) in millivolts. Excitation is a 10 Hz square waveform superimposed on a DC component to keep the total signal always positive. Voltage is kept slightly above zero during the off period. Oscilloscope and lock in amplifier coupling settings should be switched to “DC coupling” to avoid signal distortion. In a similar manner, strain with a constant rate can be applied for time t equal to half of a period and then reversed, by means of a triangular (saw-

tooth) excitation waveform as shown on the right plot of fig B.1. By imposing short constant rate strains in one or alternating directions, one can perform a stress growth after start-up or **start-up shear** and **reverse** rheometrical tests respectively.

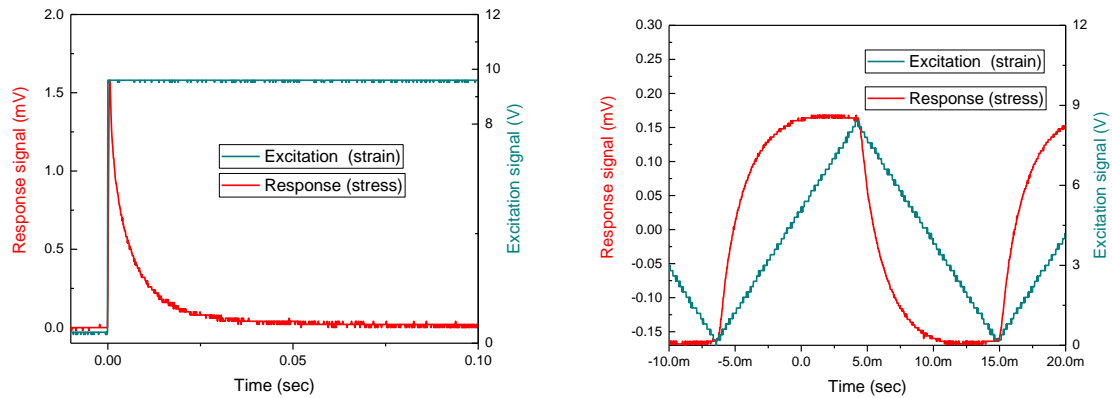


Figure B.1 Transient tests excitation (cyan) and response (red) signals. Left: Step strain test with the excitation signal being a pulse with sufficiently long period. Right: Constant strain rate test. The imposed strain is recovered after half period of the saw-tooth excitation signal.

There are numerous excitation patterns and obviously tests that can be performed. Careful usage of filters in the charge amplifier will minimize signal distortion as the contained sinusoids (Fourier) components are phase shifted according to their frequency. Finally stress/strain relation can be visualized in real time, by means of XY oscilloscope plots termed as Lissajous plots.

References

- Adrian, D. W. and A. J. Giacomin (1992). "The quasi - periodic nature of a polyurethane melt in oscillatory shear." Journal of Rheology **36**(7): 1227-1243.
- Ballesta, P. and G. Petekidis (2016). "Creep and aging of hard-sphere glasses under constant stress." Phys Rev E **93**: 042613.
- Ballesta, P., G. Petekidis, L. Isa, W. C. K. Poon and R. Besseling (2012). "Wall slip and flow of concentrated hard-sphere colloidal suspensions." Journal of Rheology **56**(5): 1005-1037.
- Bard, A. J. (1980). LR Faulkner Electrochemical Methods, Wiley, New York.
- Bartolino, R. and G. Durand (1977). "Plasticity in a Smectic-ALiquid Crystal." Physical Review Letters **39**(21): 1346-1349.
- Baumgärtel, M. and N. Willenbacher (1996). "The relaxation of concentrated polymer solutions." Rheologica acta **35**(2): 168-185.

- Bazghaleh, M., S. Grainger, B. Cazzolato, T. F. Lu and R. Oskouei (2014). "Implementation and analysis of an innovative digital charge amplifier for hysteresis reduction in piezoelectric stack actuators." Rev Sci Instrum **85**(4): 045005.
- Beenakker, C. (1984). "The effective viscosity of a concentrated suspension of spheres (and its relation to diffusion)." Physica A: Statistical Mechanics and its Applications **128**(1-2): 48-81.
- Berthier, L., G. Biroli, J.-P. Bouchaud, L. Cipelletti and W. van Saarloos (2011). Dynamical heterogeneities in glasses, colloids, and granular media, OUP Oxford.
- Bharadwaj, N. A. and R. H. Ewoldt (2015). "Single-point parallel disk correction for asymptotically nonlinear oscillatory shear." Rheologica Acta **54**(3): 223-233.
- Booij, H. and G. Thoone (1982). "Generalization of Kramers-Kronig transforms and some approximations of relations between viscoelastic quantities." Rheologica Acta **21**(1): 15-24.
- Bryant, G., S. R. Williams, L. Qian, I. K. Snook, E. Perez and F. Pincet (2002). "How hard is a colloidal "hard-sphere" interaction?" Phys Rev E Stat Nonlin Soft Matter Phys **66**(6 Pt 1): 060501.
- Chang, L., K. Friedrich, A. K. Schlarb, R. Tanner and L. Ye (2010). "Shear-thickening behaviour of concentrated polymer dispersions under steady and oscillatory shear." Journal of Materials Science **46**(2): 339-346.
- Chatzigiannakis, E., M. Ebrahimi, M. H. Wagner and S. G. Hatzikiriakos (2016). "Wall slip of polyisobutylenes: effect of molecular characteristics." Rheologica Acta **56**(2): 85-94.
- Chen, L.-S., J.-Y. Yen, J. J. H. Chen, F.-C. Kuo, M.-S. Chen, Y.-Y. Chen and B.-I. Chung (2013). "Precision tracking of a piezo-driven stage by charge feedback control." Precision Engineering **37**(4): 793-804.
- Cheng, Z., J. Zhu, P. M. Chaikin, S. E. Phan and W. B. Russel (2002). "Nature of the divergence in low shear viscosity of colloidal hard-sphere dispersions." Phys Rev E Stat Nonlin Soft Matter Phys **65**(4 Pt 1): 041405.
- Cloitre, M. and R. T. Bonnecaze (2017). "A review on wall slip in high solid dispersions." Rheologica Acta **56**(3): 283-305.
- Dealy, J. and D. Plazek (2009). "Time-temperature superposition—a users guide." Rheol. Bull **78**(2): 16-31.
- Dhont, J. K. (1996). An introduction to dynamics of colloids, Elsevier.
- Dieulesaint, E. and D. Royer (1980). Elastic waves in solids: Applications to signal processing, John Wiley & Sons.
- Edgeworth, R., B. Dalton and u. T. Parnell (1984). "The pitch drop experiment." European Journal of Physics **5**(4): 198.
- Eggers, F. and K.-H. Richmann (1995). "Oscillating plate viscometer in the Hz to kHz range." Rheologica acta **34**(5): 483-495.
- El Rifai, O. M. and K. Youcef-Toumi (2004). "Modeling of Piezoelectric Tube Actuators."
- Elliott, S. L. and W. B. Russel (1998). "High frequency shear modulus of polymerically stabilized colloids." Journal of Rheology **42**(2): 361-378.

- Evans, R. M., M. Tassieri, D. Auhl and T. A. Waigh (2009). "Direct conversion of rheological compliance measurements into storage and loss moduli." Phys Rev E Stat Nonlin Soft Matter Phys **80**(1 Pt 1): 012501.
- Ferry, J. D. (1980). Viscoelastic properties of polymers, John Wiley & Sons.
- Fritz, G., W. Pechhold, N. Willenbacher and N. J. Wagner (2003). "Characterizing complex fluids with high frequency rheology using torsional resonators at multiple frequencies." Journal of Rheology **47**(2): 303-319.
- Graessley, W. W. (2008). Polymeric liquids and networks: dynamics and rheology, Garland Science.
- Guan, J., B. Wang and S. Granick (2014). "Even hard-sphere colloidal suspensions display fickian yet non-gaussian diffusion." ACS nano **8**(4): 3331-3336.
- Hatzikiriakos, S. G. (2015). "Slip mechanisms in complex fluid flows." Soft Matter **11**(40): 7851-7856.
- Hecksher, T., D. H. Torchinsky, C. Klieber, J. A. Johnson, J. C. Dyre and K. A. Nelson (2017). "Toward broadband mechanical spectroscopy." Proc Natl Acad Sci U S A **114**(33): 8710-8715.
- Ikeda, A., L. Berthier and P. Sollich (2013). "Disentangling glass and jamming physics in the rheology of soft materials." Soft Matter **9**(32): 7669.
- Jiang, T. and C. F. Zukoski (2014). "Dynamic localization and shear-induced hopping of particles: A way to understand the rheology of dense colloidal dispersions." Journal of Rheology **58**(5): 1277-1299.
- Kirschenmann, L. and W. Pechhold (2002). "Piezoelectric Rotary Vibrator (PRV) – a new oscillating rheometer for linear viscoelasticity." Rheologica Acta **41**(4): 362-368.
- Kobelev, V. and K. S. Schweizer (2005). "Strain softening, yielding, and shear thinning in glassy colloidal suspensions." Physical Review E **71**(2): 021401.
- Koumakis, N., A. B. Schofield and G. Petekidis (2008). "Effects of shear induced crystallization on the rheology and ageing of hard sphere glasses." Soft Matter **4**(10): 2008.
- Kubo, R. (1966). "The fluctuation-dissipation theorem." Reports on progress in physics **29**(1): 255.
- Kwasniewski, P., A. Fluerasu and A. Madsen (2014). "Anomalous dynamics at the hard-sphere glass transition." Soft Matter **10**(43): 8698-8704.
- Larson, R. G., T. Sridhar, L. G. Leal, G. H. McKinley, A. E. Likhtman and T. C. B. McLeish (2003). "Definitions of entanglement spacing and time constants in the tube model." Journal of Rheology **47**(3): 809-818.
- Läuger, J. and H. Stettin (2016). "Effects of instrument and fluid inertia in oscillatory shear in rotational rheometers." Journal of Rheology **60**(3): 393-406.
- Lee, Y. S. and N. J. Wagner (2003). "Dynamic properties of shear thickening colloidal suspensions." Rheologica Acta **42**(3): 199-208.
- Likhtman, A. E. and T. C. McLeish (2002). "Quantitative theory for linear dynamics of linear entangled polymers." Macromolecules **35**(16): 6332-6343.

- Lionberger, R. A. and W. Russel (2000). "Microscopic theories of the rheology of stable colloidal dispersions." Advances in Chemical Physics **111**: 399-474.
- Lionberger, R. A. and W. B. Russel (1994). "High frequency modulus of hard sphere colloids." Journal of Rheology **38**(6): 1885-1908.
- Liu, C., J. He, E. v. Ruymbeke, R. Keunings and C. Bailly (2006). "Evaluation of different methods for the determination of the plateau modulus and the entanglement molecular weight." Polymer **47**(13): 4461-4479.
- Macosko, C. W. (1994). Rheology: principles, measurements, and applications, Wiley-vch.
- Martinoty, P., J. Gallani and D. Collin (1998). "Hydrodynamic and Nonhydrodynamic Behavior of Layer-Compression Modulus B at the Nematic-Smectic-A Phase Transition in 8 OCB." Physical review letters **81**(1): 144.
- Mason, T. G. and D. A. Weitz (1995). "Linear viscoelasticity of colloidal hard sphere suspensions near the glass transition." Phys Rev Lett **75**(14): 2770-2773.
- Mattarelli, M., M. Montagna, T. Still, D. Schneider and G. Fytas (2012). "Vibration spectroscopy of weakly interacting mesoscopic colloids." Soft Matter **8**(15): 4235.
- McKenna, G. B. (2006). "Commentary on rheology of polymers in narrow gaps." Eur Phys J E Soft Matter **19**(1): 101-108; discussion 109-111.
- Mewis, J. and P. Haene (1993). Prediction of rheological properties in polymer colloids. Macromolecular Symposia, Wiley Online Library.
- Mewis, J. and N. J. Wagner (2012). Colloidal suspension rheology, Cambridge University Press.
- Mirigian, S. and K. S. Schweizer (2014). "Elastically cooperative activated barrier hopping theory of relaxation in viscous fluids. I. General formulation and application to hard sphere fluids." J Chem Phys **140**(19): 194506.
- Morrison, F. A. (2001). "Understanding Rheology. 2001." Ox. Un. Press, ISBN: 978-970.
- Morrison, R. (1967). "Grounding and shielding techniques in instrumentation." New York: Wiley, 1967.
- Müller, G., M. Weber, G. Rumpker and D. Gajewski (2007). Theory of elastic waves, Geoforschungszentrum.
- Negi, A. S. and C. O. Osuji (2010). "Time-resolved viscoelastic properties during structural arrest and aging of a colloidal glass." Phys Rev E Stat Nonlin Soft Matter Phys **82**(3 Pt 1): 031404.
- Nemirovsky, Y., A. Nemirovsky, P. Murali and N. Setter (1996). "Design of novel thin-film piezoelectric accelerometer." Sensors and Actuators A: Physical **56**(3): 239-249.
- Parot, J. M. and B. Duperray (2007). "Applications of exact causality relationships to materials dynamic analysis." Mechanics of Materials **39**(5): 419-433.
- Pham, K., S. Egelhaaf, P. Pusey and W. C. Poon (2004). "Glasses in hard spheres with short-range attraction." Physical Review E **69**(1): 011503.
- Plazek, D. J. (1996). "1995 Bingham Medal Address: Oh, thermorheological simplicity, wherefore art thou?" Journal of Rheology **40**(6): 987-1014.

- Polanowski, P. and A. Sikorski (2017). "Comparison of different models of motion in a crowded environment: a Monte Carlo study." Soft Matter **13**(8): 1693-1701.
- Preumont, A. (2006). Mechatronics, Springer.
- Pusey, P. (1991). "Colloidal Suspensions in Liquids, Freezing, and the Glass Transition: Les Houches."
- Pusey, P. (2008). "Colloidal glasses." Journal of Physics: Condensed Matter **20**(49): 494202.
- Pusey, P. N. (2011). "Brownian motion goes ballistic." Science **332**(6031): 802-803.
- Riggs, P. J. (2009). Quantum causality: conceptual issues in the causal theory of quantum mechanics, Springer Science & Business Media.
- Roth, M., M. D'Acunzi, D. Vollmer and G. K. Auernhammer (2010). "Viscoelastic rheology of colloid-liquid crystal composites." The Journal of chemical physics **132**(12): 124702.
- Rouleau, L., J. F. Deü, A. Legay and F. Le Lay (2013). "Application of Kramers–Kronig relations to time–temperature superposition for viscoelastic materials." Mechanics of Materials **65**: 66-75.
- Royall, C. P., W. C. K. Poon and E. R. Weeks (2013). "In search of colloidal hard spheres." Soft Matter **9**(1): 17-27.
- Rubinstein, M. and R. H. Colby (2003). Polymer physics, Oxford University Press New York.
- Russel, W. B., N. J. Wagner and J. Mewis (2013). "Divergence in the low shear viscosity for Brownian hard-sphere dispersions: At random close packing or the glass transition?" Journal of Rheology **57**(6): 1555-1567.
- Saltzman, E. J. and K. S. Schweizer (2006). "Activated hopping and dynamical fluctuation effects in hard sphere suspensions and fluids." J Chem Phys **125**(4): 44509.
- Sánchez, A. M., R. Prieto, M. Laso and T. Riesgo (2008). "A piezoelectric minirheometer for measuring the viscosity of polymer microsamples." IEEE Transactions on Industrial Electronics **55**(1): 427-436.
- Schrag, J. L. (1977). "Deviation of velocity gradient profiles from the “gap loading” and “surface loading” limits in dynamic simple shear experiments." Transactions of the Society of Rheology **21**(3): 399-413.
- Schwarzl, F. and A. J. Staverman (1952). "Time - Temperature Dependence of Linear Viscoelastic Behavior." Journal of Applied Physics **23**(8): 838-843.
- Schweizer, K. S. and E. J. Saltzman (2003). "Entropic barriers, activated hopping, and the glass transition in colloidal suspensions." The Journal of Chemical Physics **119**(2): 1181-1196.
- Schweizer, K. S. and G. Yatsenko (2007). "Collisions, caging, thermodynamics, and jamming in the barrier hopping theory of glassy hard sphere fluids." The Journal of chemical physics **127**(16): 164505.
- Shikata, T. and D. S. Pearson (1994). "Viscoelastic behavior of concentrated spherical suspensions." Journal of Rheology **38**(3): 601-616.

- Siebenbürger, M., M. Ballauff and T. Voigtmann (2012). "Creep in colloidal glasses." Physical review letters **108**(25): 255701.
- Sierou, A. and J. F. Brady (2001). "Accelerated Stokesian Dynamics simulations." Journal of Fluid Mechanics **448**.
- Sirohi, J. and I. Chopra (2016). "Fundamental Understanding of Piezoelectric Strain Sensors." Journal of Intelligent Material Systems and Structures **11**(4): 246-257.
- Swan, J. W. and R. N. Zia (2013). "Active microrheology: Fixed-velocity versus fixed-force." Physics of Fluids **25**(8): 083303.
- Szántó, L., R. Vogt, J. Meier, D. Auhl, E. Van Ruymbeke and C. Friedrich (2017). "Entanglement relaxation time of polyethylene melts from high-frequency rheometry in the mega-hertz range a." Journal of Rheology **61**(5): 1023-1033.
- Thorneywork, A. L., R. E. Rozas, R. P. Dullens and J. Horbach (2015). "Effect of Hydrodynamic Interactions on Self-Diffusion of Quasi-Two-Dimensional Colloidal Hard Spheres." Phys Rev Lett **115**(26): 268301.
- Tschoegl, N. W. (2012). The phenomenological theory of linear viscoelastic behavior: an introduction, Springer Science & Business Media.
- van de Laar, T., R. Higler, K. Schroen and J. Sprakel (2016). "Discontinuous nature of the repulsive-to-attractive colloidal glass transition." Sci Rep **6**: 22725.
- Velankar, S. and D. Giles (2007). "How do I know if my phase angles are correct?" Rheol. Bull **76**(8).
- Vlassopoulos, D. (2016). "Macromolecular topology and rheology: beyond the tube model." Rheologica Acta **55**(8): 613-632.
- Vlassopoulos, D. and M. Cloitre (2014). "Tunable rheology of dense soft deformable colloids." Current Opinion in Colloid & Interface Science **19**(6): 561-574.
- Vleminckx, G. and C. Clasen (2014). "The dark side of microrheology: Non-optical techniques." Current Opinion in Colloid & Interface Science **19**(6): 503-513.
- Wagner, N. J. (1993). "The high-frequency shear modulus of colloidal suspensions and the effects of hydrodynamic interactions." Journal of colloid and interface science **161**(1): 169-181.
- Wang, G., G. Chen and F. Bai (2015). "High-speed and precision control of a piezoelectric positioner with hysteresis, resonance and disturbance compensation." Microsystem Technologies **22**(10): 2499-2509.
- Wang, X., V. Pommier-Budinger, A. Reysset and Y. Gourinat (2014). "Simultaneous compensation of hysteresis and creep in a single piezoelectric actuator by open-loop control for quasi-static space active optics applications." Control Engineering Practice **33**: 48-62.
- Wang, Y.-Z., G.-H. Wang, X.-M. Xiong, B. Wang, L.-M. Zhang and J.-X. Zhang (2010). "Viscoelastic measurement of complex fluids using forced oscillating torsion resonator with continuously varying frequency capability." Rheologica Acta **49**(11-12): 1117-1126.
- Weeks, E. R. (2017). "Introduction to the Colloidal Glass Transition." ACS Macro Letters **6**(1): 27-34.

Weeks, E. R., J. C. Crocker, A. C. Levitt, A. Schofield and D. A. Weitz (2000). "Three-dimensional direct imaging of structural relaxation near the colloidal glass transition." Science **287**(5453): 627-631.

Weeks, E. R. and D. Weitz (2002). "Subdiffusion and the cage effect studied near the colloidal glass transition." Chemical physics **284**(1): 361-367.

Wen, Y. H., J. L. Schaefer and L. A. Archer (2015). "Dynamics and Rheology of Soft Colloidal Glasses." ACS Macro Letters **4**(1): 119-123.

Willenbacher, N. and C. Oelschlaeger (2007). "Dynamics and structure of complex fluids from high frequency mechanical and optical rheometry." Current Opinion in Colloid & Interface Science **12**(1): 43-49.

Winter, H. H. (1997). "Analysis of dynamic mechanical data: inversion into a relaxation time spectrum and consistency check." Journal of Non-Newtonian Fluid Mechanics **68**(2-3): 225-239.

Yamamoto, J., H. Nakamura and K. Okano (1987). "Apparatus for Measurement of Complex Shear Modulus of Liquid Crystals at Low Frequencies." Japanese Journal of Applied Physics **26**(S1): 29.

Yamamoto, J. and K. Okano (1991). "Anomalous hydrodynamic behaviors of smectic liquid crystals at low frequencies." Japanese journal of applied physics **30**(4R): 754.

Yang, K. and W. Yu (2017). "Dynamic wall slip behavior of yield stress fluids under large amplitude oscillatory shear." Journal of Rheology **61**(4): 627-641.

Yi, K. A. and R. J. Veillette (2005). "A charge controller for linear operation of a piezoelectric stack actuator." IEEE transactions on control systems technology **13**(4): 517-526.

Yoshimura, A. S. and R. K. Prud'homme (1988). "Wall Slip Effects on Dynamic Oscillatory Measurements." Journal of Rheology **32**(6): 575-584.

Zaccarelli, E., S. M. Liddle and W. C. Poon (2015). "On polydispersity and the hard sphere glass transition." Soft Matter **11**(2): 324-330.